Summer 8-2020

Energy Harvesting Using Flextensional Piezoelectric Energy Harvesters in Resonance and Off-Resonance Modes

Mohamed A. Shabara
Old Dominion University, shabara91@gmail.com

ENERGY HARVESTING USING FLEXTENSIONAL PIEZOELECTRIC ENERGY HARVESTERS IN RESONANCE AND OFF RESONANCE MODES

by

Mohamed A. Shabara
M.Sc. February 2018, Alexandria University, Egypt
B.Sc. June 2013, Alexandria University, Egypt

A Thesis Submitted to the Faculty of
Old Dominion University in Partial Fulfillment of the
Requirements for the Degree of

MASTER OF SCIENCE

MECHANICAL AND AEROSPACE ENGINEERING

OLD DOMINION UNIVERSITY
August 2020

Approved by:

Tian-Bing Xu (Director)

Gene Hou (Member)

Mileta Tomovic (Member)

ABSTRACT

ENERGY HARVESTING USING FLEXTENSIONAL PIEZOELECTRIC ENERGY HARVESTERS IN RESONANCE AND OFF RESONANCE MODES

Mohamed A. Shabara
Old Dominion University, 2020
Director: Dr. Tian-Bing Xu

Energy harvesting technologies are integrated into various modern devices and systems. These systems include Artificial Intelligence (AI) systems, Internet of Things (IoT), various types of energy harvesters are integrated in many engineering applications such as automotive, aerospace and ocean engineering. In order to develop a fully functioning stand-alone system, it is essential to integrate it with a built in power source such as a battery or a power generator. Also, in many situations, city power sources might not be available. Therefore, reliable, renewable and sustainable local power generators are desired. Piezoelectric energy harvesting (PEH) technologies, which are piezoelectric material-based devices, are one of the best candidates for this job. Piezoelectric energy harvesters convert mechanical energy from vibrating or moving objects to electrical energy. These devices have the highest capability of designing self-powered systems as they are not weather dependent and they are capable of harvesting both small or large mechanical movements into electrical energy. The piezoelectric materials are materials that generate electrical charges when mechanical stress or force is exerted on them. On the other hand, they deform when an electric voltage is applied to them. The piezoelectric-based energy harvesters are small and effective devices that promise future engineering systems to be more intelligent, reliable and environmentally friendly. Designing a piezoelectric device is cumbersome, and it is indispensable to have a comprehensive understating of many engineering disciplines before delving into designing a new device or redesigning an existing device. These disciplines include mechanical engineering, electrical engineering, materials sciences, and device physics. In this

thesis, comprehensive mathematical and experimental investigations were done for modeling piezoelectric multi-later stacks and Flextensional Energy Harvesters in resonance and in off-resonance modes. For the resonance mode, mathematical and variational approaches were used to modeling a selected piezoelectric multi-layer stack found in the market; the models are a static model, single degree of freedom model (SDOF), a distributed parameter model and a finite element model for the resonance mode, a finite element model (using ANSYS) was used to model a single and a multiple stage Flexteisonal Energy Harvester. To validate off-resonance results, previously published experimental results were used; however, for the resonance mode an experiment was carried out to validate the numerical model's results for the multi-stage Energy Harvester. As for the single stage Flextensional Energy Harvester, previously published experimental results were used to validate the finite element model. The advantages and disadvantages of different models and approaches are compared and discussed.

To my family.

ACKNOWLEDGMENTS

First and foremost, all praise be to almighty Allah, for His countless blessings and guidance. During the course of this work, Prof. Tian-Bing Xu, has provided so much effort and dedication. Without his help and brilliant guidance this work would have been immeasurably more difficult. I would like to express my sincerest gratitude to him. I want to thank him for the long days and midnight meetings and for his tolerance for long emails, meetings and calls. I will never forget his continuous support. I feel deeply honored to be his student.

I am also extremely grateful to my managers at my previous work in Egypt, Mohamed Sobhy, Ibrahim Arafa, Ibrahim Saleh and Yasser Barakat, for their continuous support and understanding.

My time at Old Dominion University as a graduate student would have been less interesting and satisfying without all my friends' help and support. To name just a few, I would like to give my thanks to my class mates/roommates AbdulRahman AlBadawy and Hisham AbuSalma. Without them my time away from my home country wouldn't be the same.

I would like to express my profound gratitude to my family. I owe everything to the unconditional love and support I got from my parents, Ahmed and Gihan. To the encouragement of my brother Yahia and the everlasting demands of my young sisters Amal and Yousra.

TABLE OF CONTENTS

Page

LIST OF TABLES

LIST OF FIGURES

Figure Page

NOMENCLATURE

α	Frame's Force Amplification Factor
$\ddot{x}$	Acceleration
$\dot{x}$	Velocity
ϵ_0	The dielectric permissivity of free space (8.854×10^{-12}) "F/m"
ϵ_{33}^{σ}	Dielectric Permitting at Constant Stress
ω_n	Natural Frequency
ω_{nd}	Damped Frequency
σ	Stress
ζ_n	Damping Ratio
A	Surface Area
Amp	Amplitude
D	Electric Displacement Vector
d_{33}	Piezoelectric Constant "C/N"
d_{ij}	Piezoelectric Charge Constant
e_{ij}	Piezoelectric Stress Coefficient
E_{RMS}	Root mean square error "%"
En	Generated Energy
F	Force
f	frequency "Hz"
i	Current "$Ampere$"
L	Length of the Stack

M Mass "kg"

n_s Number of Stages

p Number of Piezoelectric Layers

Q Electric Charge "$Coulomb$"

R Electric Resistance "Ohm"

R_{ESR} Equivalent Serial Resistive

S Strain

s_{ij}^{E} Compliance Coefficient

t Time "sec"

t_p Layer Thickness

$tan(\delta)$ Dielectric Loss

V Voltage "$Volts$"

x Displacement

Y Young's Modulus of Elasticity

FPEH Flextensional Piezoelectric Energy Harvesters

MFAPEHT Multistage Force Amplification Piezoelectric Harvester Transducer

PEH Piezoelectric Energy Harvesters

SDOF Single Degree of Freedom

VIV Vortex Induced Vibrations

CHAPTER 1

INTRODUCTION

The compelling need for building self-powered systems, aerospace applications, wireless sensors networks (WSNs) [1], robots, artificial intelligence (AI) systems, etc. lead to the discovery of many energy harvesting techniques and devices that convert thermal energy [2, 3] (thermoelectric, pyroelecric, etc), light energy [4] (photovoltaic, etc), chemical energy and mechanical energy [5, 6, 7, 8] (piezoelectric, triboelectric, etc.) into electrical energy. However, most of those energy harvesting technologies are weather dependent. Mechanical energy from vibration is unique in that it is not weather dependent. Shabara et al. [9] carried out a comprehensvie investigation on the recent designs of piezoelectric energy harvesters and their corresponding power outputs. [1].

Converting mechanical vibration/motion energy can be accomplished using either piezoelectric materials [10, 11, 12, 13, 14], electro-magnetic field [15, 16, 17] (ex: RF energy harvesting) and electrostatic [11, 18]. Among those, the advantage of piezoelectric energy harvesting is that it can harvest mechanical energy produced by the minimal motion (down to nano-scale movement). Piezoelectric energy harvesters are often classified into 3 categories [19] (i) macro-miso scale harvesters [20, 21], (ii) Micro-Electro-Mechanical Systems or MEMS scale [22, 23, 24, 25] (iii) nano-scale [26, 27, 28] depending on their weight, size, power output, manufacturing method and application field.

Modern engineering applications such as artificial intelligence (AI) (also called machine intelligence), which was initially developed in computer science, is the ability of a computer or a machine to stimulate consistent with traditional responses from humans, given the human capacity for contemplation, judgment, and intention without human interference. Now, AI is used broadly in machines that mimic human cognition [29, 30]; the leap forward in the field of electronic devices, wireless communication and artificial intelligence technologies resulted in a compelling need to develop more energy efficient and reliable systems. The advancement in artificial intelligence systems and big data and the replacement of conventional systems [31, 32, 33]. The AI is implemented in animal-inspired robots [34], humanoid robots [35, 36], internet of things (IoT) [37, 38]. The components of the aforementioned

[1]Some passages have been quoted verbatim from Shabara et al. [9]

systems required local power generation for the control systems, actuators, wireless sensors as well as wireless condition monitoring systems, these power generators must be portable and miniaturized reach the nano-scale (nanogenerators). One challenge of the practical application of AI systems is having reliable and renewable local power sources for the hardware to make it power independent. That enables the integrated self-powered computer, sensor network, actuators, and wireless communication of the AI system to act as a sustainable natural intelligent system in real world. Recently, the developed various energy harvesting technologies might provide solutions to overcome those challenges.

Arms et al. [39] proposed a smart piezoelectric self-powered wireless sensor that senses temperature and humidity, a piezoelectric cantilever harvester beam was used to power the sensor, the microprocessor, the on-board memory and a rechargeable battery. They used techniques that enabled this device to consume low power that ranged from 90 to 900 μW. These techniques included using sleep mode between sampling periods, signals that triggers the device between sample and recording/transmitting the sensor readings average data instead of the frequency transmitting, etc.

Since 2000s, various attempts and contributions have been performed to maximize the harvested energy as well as the energy conversion efficiency and practicality of the Piezoelectric Energy Harvesters (PEH). The prefix of piezoelectric came from the Greek word *piezein* which means press or squeeze. This material property was firstly discovered in 1880 by Paul-Jacques Curie in quartz ceramic. The attempts varied from trying to enhance the transmitted mechanical energy from the source of vibration to the piezoelectric material or maximizing the produced electric charges, collecting and storing the produced electric energy, and miniaturizing the PEH size to obtain high specific energy destiny (harvested energy per harvester volume).

Roundy [40] listed some mechanical vibration sources with their peak acceleration and vibration frequency that can be the source of excitation for energy harvesting devices. Also, Sue et al. [41] carried out a comprehensive study on the human body activities and movements that could be used in energy harvesting applications which can be implemented in humanoid robots.

Abdelkefi [10] reviewed various devices, linear, non-linear, theoretical models and experimental models in the applications of aeroelastic energy harvesting; the review gave a thorough investigation of energy harvesting from fluttering energy, vortex induced vibrations (VIV), galloping in structures using fluttering harvesters, cylindrical energy harvesters, flapping leaf-flap, galloping and wave galloping energy harvesters as well as other harvesters'

types.

This introductory chapter will be divided into four sections. The first section will review the piezoelectric materials from the time of their discovery to the past decade's inventions and breakthroughs. Then, in the second subsection we will review the three designs of flexnesional piezoelectric energy harvesters (FPEH); the three reviewed designs are Circular cymbal, the Circular Diaphragm and "33" mode Piezoelectric Multilayer Stacked Flextensional PEHs.

1.1 PIEZOELECTRIC MATERIALS

Piezoelectric materials belong to a bigger family of materials called "smart materials". Smart materials react to a certain input that is applied on them with a difference it in the form of stress, electric field, magnetic field, heat or light with an output in the form of strain, magnetization, charge, current, temperature or light as defined by Uchino [42]. The electric-mechanical (E-M) energy conversion effect is called piezoelectric effect. Piezoelectric materials can be further classified into non-organic piezoelectric materials (piezoceraics) and organic piezoelectric materials (piezopolymers).

French physicists and brothers Jacques and Pierre Curie were the first to discover the piezoelectric effect in 1880 when they were investigating quartz. Since that time and until 1964, no significant discovery was made. In 1946, Barium Titanite "$BaTiO_3$" was discovered. Researchers consider it the first manufactured piezocermaic [43, 44]. "$BaTiO_3$" has two forms, either a ferroelectric or non-ferroelectric form depending on the temperature of operation. The difference between these two forms is made at the so-called Curie temperature. The discovery of the Barium Titanate was a breakthrough in the smart materials field due to its unprecedented high electro-mechanical coupling factor [45] at that time which opened the door for more piezoelectric discoveries. In 1954, Jaffe et al. [46] discovered the inorganic perovskite compounds named lead zirconate Titanite ceramics (PZT). Currently, the coupling factor of the PZT ceramics can reach as high as 75%.

In 1960s, the lead-free PZT ceramics Bismuth Sodium Titanite (BNT) [47], an inorganic compound that conforms with the perovskite structure, were discovered. The Perovskite structure is named after the Russian mineralogist L. A. Perovski [48] and is defined as a crystal that has anion atoms (ions with extra electrons $-ve$) in the corners (in our case its Oxygen atoms), and it follows the formula ACX_3, where A and B atoms resembles the cation (ions with lesser electrons $-ve$) with different sizes, usually A is larger than B ions [49]. With the beginning of the 21^{st} century further advancements and innovation were done

in the field of piezoelectric materials that lead to the development KNN, BT, BNT, BFO based ceramics.

In the past 3 decades, great effort was done by researchers trying to develop piezoelectric signal crystal materials "also known as relaxors". Some examples for relaxors are $Pb(Mg_{1/3}Nb_{2/3})$ 1-$xTixO_3$ (PMN-PT) [50, 51], $Pb(In_{1/2}Nb_{1/2})O_3$ – $Pb(Mg_{1/3}Nb_{2/3})O_3$ - $PbTiO_3$ (PIN-PMN-PT), $Pb(Zn_{1/3}Nb_{2/3})O_3$-$PbTiO_3$ (PZN-PT), which have significant advantages over the common piezoelectric ceramic [52]. The electromechanical coupling effects can be as high as 96% and the piezoelectric ecoefficiency as high as 3500. Since Kawai discovered strong piezoelectric effect in poly(vinylidene fluoride) (PVDF), various piezoelectric polymeric materials have been developed, such as Poly(vinylidenefluoride-trifluoroethylene) P(VDF-TrFE) copolymer [52, 53], poly(vinylidene fluoride-trifluoroethylene-clorotrifluoroethylene) [P(VDF-TrFE-CTFE)] terpolymer [54], odd nylons, polyamides [55], and polymeric composites.

1.2 FLEXTENSIONAL PIEZOELECTRIC HARVESTERS

The first reported flextensional PEH was proposed by Kim et al. [56] at Penn State University, the flextensional harvesters are known to produce higher power compared to the other types of harvesters. In this section we focus on 3 types of Flextensioal energy harvesters namely the circular cymbal, "33" and circular diaphragm mode FEHs. The Flextensional harvesters are known to produce power outputs of at least 1 order of magnitude higher compared to other harvesters types.

Circular Cymbal

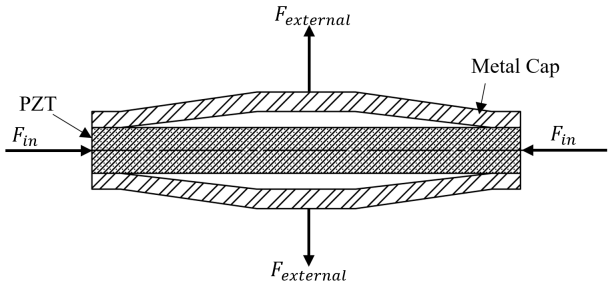

Fig. 1: Cymbal harvesters, piezoelectric disk sandwiched between a pair of concaved metal caps

The Cymbal harvester succeeded in achieving efficiency of 7.8% which was a break through at that time [62]. The circular Cymbal harvesters, as shown in Fig. (1), are

TABLE I: A Summary of off Resonance Mode Circular Cymbal PEH

Authors	**Material**	**Dimensions (mm)**	**Power (mW)**	**Frequency (Hz)**	**Force (N)**
Kim et al. [56]	PZT	$\phi = 29$; $t = 1$	53	100	70
Kim et al. [57]	PZT	$\phi = 29$; $t = 1$	100	200	70
Uchino and Ishii [58]	PZT - 10 Layer Stack	$\phi = 29$; $t = 1$	53	100	70
Yuan et al. [59]	PZT - 10 Layer Stack	$\phi = 35$; $t = 4$	2.5	120	8.15
Palosaari et al. [60]	PZT	$\phi = 35$; $t = 0.5$	0.66	1.19	24.8

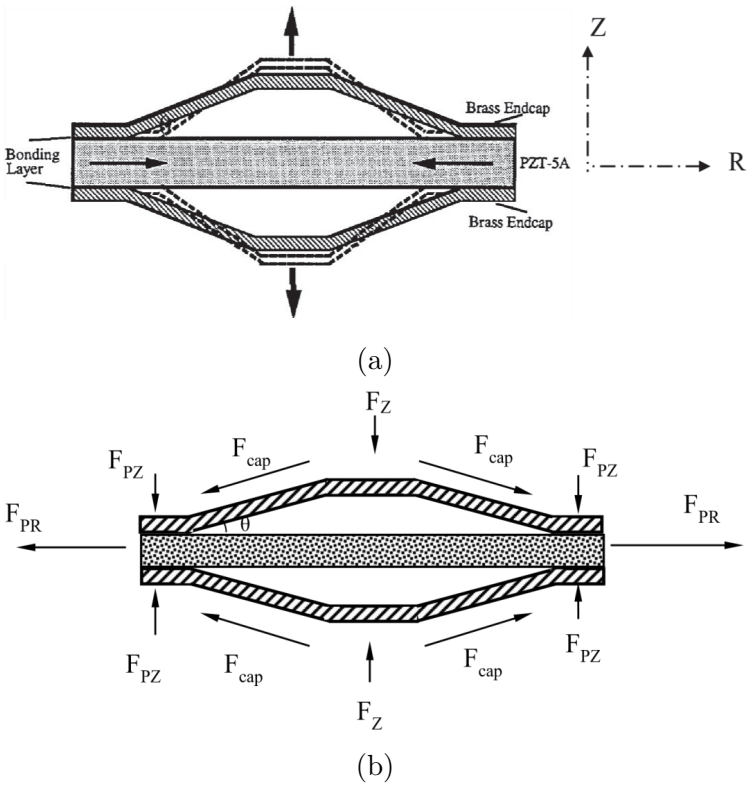

Fig. 2: Schematic Of the principle of a cymbal transducer (a)as an actuator, arrows shows displacement directions, and (b) as an energy harvester [61]

formed of a piezoelectric disk sandwiched between a pair of concaved metal caps (dome-shaped). This design amplifies the applied force/displacement and, consequently, the electrical charges. Changing the thickness of the metal caps tunes the harvester to give the desired response, the amplification factor (M) for this frame can be calculated using Eq. (1), where the angle (θ) is shown in Fig. (2). Also, electrical charges produced are a combination of both the d_{31} and the d_{33} modes which produces more electric charge compared to the most used harvesters at that time which are based only on the d_{31} which provides energy conversion efficiency as low as 10%. The effective piezoelectric constant for a circular cymbal operating on d_{31} and the d_{33} modes is shown in Eq.(2).

$$M \approx \frac{1}{\tan(\theta)} \tag{1}$$

$$d_{\text{eff}} = 1 + M \mid \frac{d_{31}}{d_{33}} \mid \tag{2}$$

In 2005, Deng et al. [63] designed a composite cymbal stack with proof mass. The biggest difference between that device and the foremost cymbal harvesters is that it used relaxor piezoeramics which have higher piezoelectric properties. Also, the response frequency of the inductance of the piezoelectric crystal is tuned to match the mechanical response of the frame and the proof-mass.

Table (I) gives a brief summary of some of the non-resonance mode circular Cymbal PEH discussed in the current thesis.

"33" Mode Piezoelectric Multilayer-stacked Flextensional PEHs

The first "33" mode energy harvester was proposed by Cedrat Technoilogies as reported by Sosnicki et al. [64] as shown in Fig. (3), this harvester was integrated with a force amplification frame (FAF); it succeeded in harvesting $50mW$ with an excitation displacement of $35\mu m$ at $100Hz$.

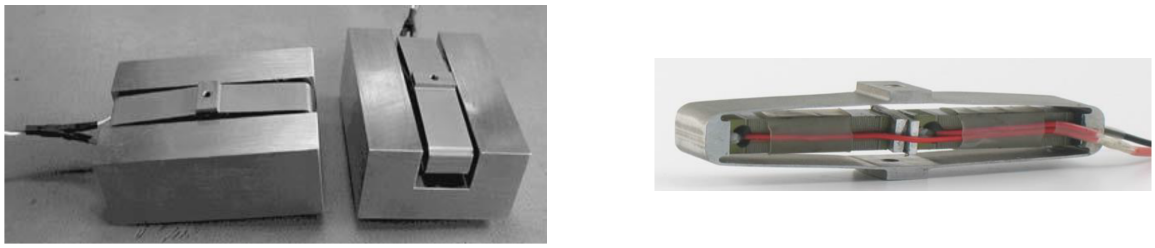

Fig. 3: Pictures of Cedrat APA400M-MD [62]

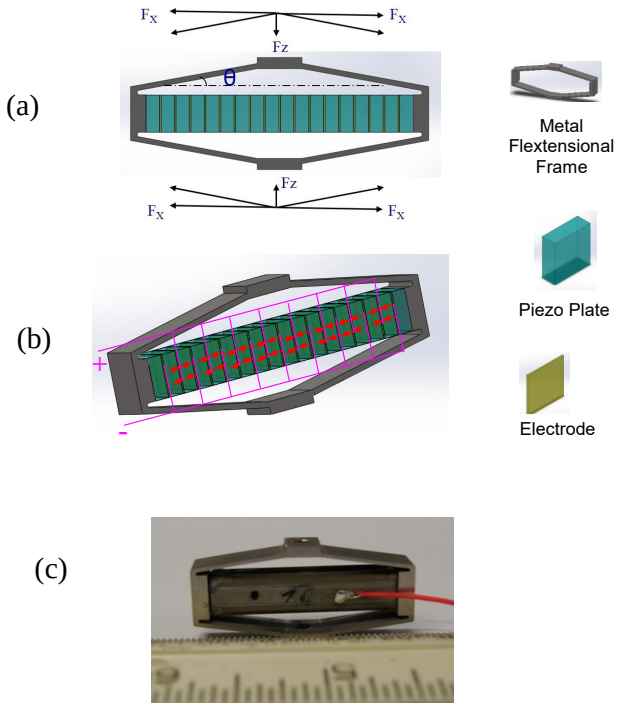

Fig. 4: Piezoelectric PZT ceramic multilayer–stacked flextensional harvester (PZT-Stacked-FEH) (a) 2D-diagram of the PZT-Stacked-FEH with applied force, (b) 3D-diagram of the PZT-Stacked-FH, and (c) the picture of the PZT-Stacked-FEH. [65]

This harvester's frame was further modified by Liu et al. [66, 67] and Bencheikh et al. [68]. The modified frame is called buckled-spring-mass (BSM) bistable harvester. It succeeded in producing $16mW$ at an acceleration of $3m/s^2$ at $26.5Hz$. Xu et al. [69] presented a multi-layer PZT-stack that converted 35% of the input energy to electric power and 70% of the generated electric power to the resistive load, and the mechanical to electrical energy conversion efficiency reached 35%. The generated power was significantly larger than the corresponding cantilever type harvesters. Feng et al. [70] proposed new analytical and first order-numerical models. The results were verified using experimental data, and the analytical model used the variational approach of Hamilton principle. The proposed model agreed with the experimental data with high accuracy.

Starner [71] considered walking as one of the most energy consuming activities a human body performs, and many attempts were made to design shoe harvesters over the past decades like the harvester designed by Shenck et al. [72], Kymissis et al. [73], Feng et al. [74, 75], Baghbani et al. [76] and Nathan [77], etc. Kymissis et al. [73] proposed one of the earliest attempts to harvest energy from a shoe. They proposed three devices that

can be implemented. The first was a unimorph strip made of piezoelectric composite; the second was a stave composed of multilayer PVDF foils while the third device was a magnet based generator which generated higher power than the piezoelectric based harvested which produced powers of the order of milliwatts; however, it would impair the movement of the wearer due to its size.

In 2018, Feng et al. [75] carried out numerical (ANSYS) and experimental analysis and modeled compression "33" mode harvesters with three different assemblies. The assembly is composed of a number of harvesters sandwiched between two aluminum plates and inserted in a heel. The assemblies had eight, six and four harvesters respectively tested in walking speeds of $4km/h$, $4.8km/h$ and $5.6km/h$. The assembly with four harvesters only was found to give the highest power because the applied force per harvester was larger with a maximum power of $20mW/shoe$ at the walking speed $5.6km/h$; however, using only four harvesters will expose the FAF high stresses as that frame has stress concentration regions that would make the harvester break under fatigue load.

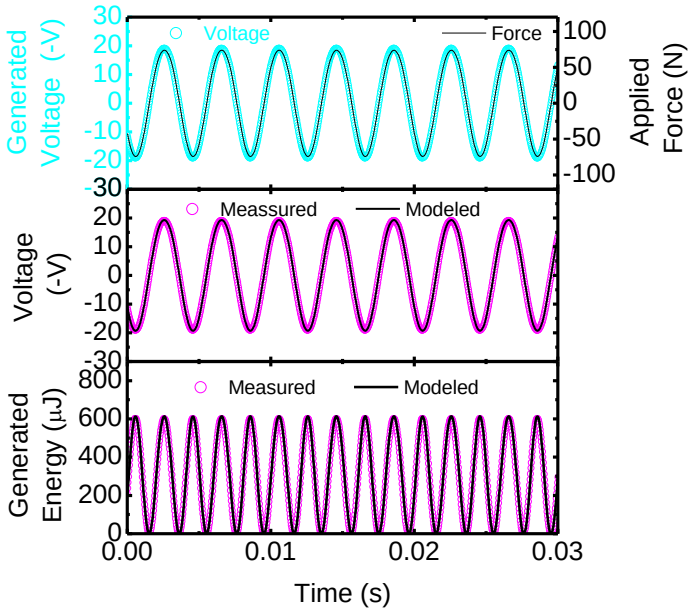

Fig. 5: Time dependent voltage, applied force, and generated energy [65]

In further extension of this work Feng et al. [74] proposed another Finite Element Analysis model using the ANSYS APDL. Full geometry and quarter geometry models were compared. The results of the quarter geometry model showed great agreement with the results of the full geometry model, which proved the applicability of applying the symmetric boundary conditions to these types of models which significantly reduces the simulation time. Also, this piezoelectric stack had 300 layers ceramic and 301 electrodes. Each layer

has a thickness of $0.1mm$ and $0.1\mu mm$ respectively. This type of geometry, small thickness geometries, can be so problematic when meshing the bodies. Accordingly, it was proposed to treat the whole piezoelectric stack as one with piezoelectric charge constant. This effective piezoelectric charge constant $\overline{d_{33}}$ can be calculated as follows

$$\overline{d_{33}} = pd_{33}. \tag{3}$$

Xu et al. [65] developed a "33" mode PZT multilayer stack-based flextensional harvester (PZT-Stacked-FEH). They designed an elastic force amplification frame (FAF) that would capture mechanical energy with a high energy transition efficiency into the (PZT-Stacked-FEH). The operation in the "33" mode allowed high mechanical to electrical energy conversion efficiency and generated more charges. The mechanical energy transmitted to the PZT-Stacked-FEH due to the FAF is magnified by a factor of 5 which generated 48.6 electrical energy times compared to without the FAF. Also, 26.5 times more electrical power was generated compared to directly applying a force to the PZT-stack as well as 19% of the overall mechanical to electrical energy efficiency was obtained. Fig. (5) below demonstrates a time dependent plot for generated voltage, applied force, and generated energy is shown. In Fig. (6) a time dependent plot of the level of voltage and stored electrical energy for 6,600 μF capacitor charged by the PZT-Stacked-FEH.

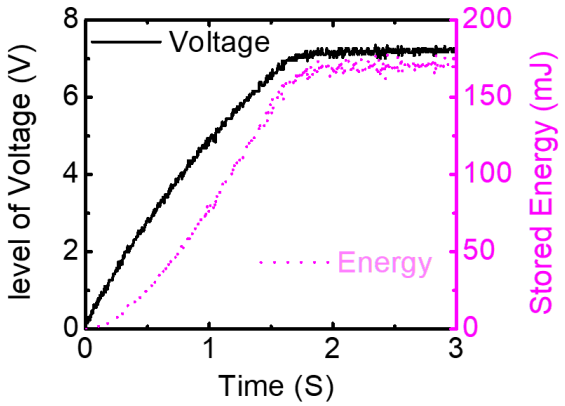

Fig. 6: Level of voltage and Energy Stored [65]

Limitation of energy harvesting from the sole of the shoe can cripple the wearer, the idea of energy harvesting backpacks became a compelling idea. The relative movement between the backpack and the person wearing it generates mechanical energy. Several attempts were made to harvest this energy and convert to useful electrical energy.

Rome et al. [78] used a suspended load backpack arrangement that harvest power of

7.37 W from the vertical movement at a walking speed of about 6.45 km/hr which is as much as 300 folds of the maximum shoe generated power at that time. Moreover, the authors reported that the power generation from a person carrying $29kg$ load reached $7.5W$. Unfortunately, this arrangement also would impair the movement of the backpack carrier due to the energy harvester degree of freedom and will lead to increased fatigue.

In 2007, Granstrom et al. [79] proposed harvesting energy from piezoelectric straps made of PVDF polymers attached to backpack straps. The tested straps had thicknesses of $28\mu m$ and $52\mu m$. One, two, three and four straps connected in parallel or in a series were tested and simulated. I was shown that the parallel connection produces more power compared to the series connection, and using one strap only produced more power. Also, it was noticed that the generated voltage high was compared to the current due to the high impedance of the PVDF material. It is worth mentioning that their numerical model assumed pure tension on the harvester and ignored the bending moments.

1.2.1 CIRCULAR DIAPHRAGM PEHS

TABLE II: Brief Summary for Some Diaphragm Piezoelectric Harvesters

Authors	**Material**	**Dimensions** (mm)	**Power** (mW)	**Power Density** (mW/cm^3)	**Frequency** (Hz)
Palosaari et al.[80]	PZT-5A	$\phi = 34.5$; $t = 0.1905$	0.96	6.06	0.96
Mo et al.[81]	PZT-5H	$\phi = 25.4$; $t = 0.127$	0.128	1.99	1
Leinonen et al.[82]	PZT-5H	$\phi = 35$; $t = 0.5$	0.784	1.63	4
Wang et al.[83]	PZT	$\phi = 35$; $t = 4$	8.5	86.58	150
Chen et al. [84]	PZT	$\phi = 35$; $t = 0.5$	12	30.56	113

Since the 1900s, the circular diaphragm (or membrane) piezoelectric transducers were investigated and used in the applications of loudspeakers and recorders, etc. [85, 86]. Most of the work in the literature focused on the applications of circular diaphragm piezoelectric devices in actuation applications such as microfluidic, optical applications [87, 88]. Recently they have been implemented in energy harvesting applications. Diaphragm PEHs are small in size and capable of working in resonance and off-resonance modes and are capable in working in low [80, 81, 82] and relatively high [84, 83, 89] frequencies ($0.9 \sim 400Hz$).

Deterre et al. [90] designed a diaphragm circular harvester that works in low frequency $(2Hz)$in fluidic environments (like blood), analytically and experimental studies were presented. A proposed optimization technique was presented to the extract collected charge by applying controlled voltage.

In 2014, Palosaari et al. [80] designed a mechanically loaded diaphragm harvester. The mechanical prestress is applied using a spring, this preload succeeded in increasing the efficiency of the harvester by 141% compared to the case of without prestress.

The Flextensional Piezoelectric Energy Harvesters are among the best and the most powerful energy harvesters on the market due to the following reasons:

- The Force Amplification Frames (FAF) are capable of greatly magnifying the input force to the piezoelectric piece. Joel et al. [79] reported one of the heights force amplification factors α which was 10. Feng et al. [74] used the biogeography-based optimization (BBO) technique to design a FAF which yields $\alpha = 8.5$. Xu et al [65] reported an amplification factor of 5.5.

  Unfortunately, while all three works used static loading to calculate the force amplification factors "α" there is no universal agreement between FAF designers for calculating "α". Joel et al. [79] used the ratio between the deformation of the harvester's top area and deformation of the piezoelectric while Feng et al.'s [74] calculation was based on the ratio between the input to the output forces. Xu et al. [65] used an analytical method to calculate the value of "α" based on the frame geometry.

- FPEHs operate in the 33 mode rather than the "31" mode, the "33" mode produces as much as twice the generated charge and $3 \sim 5$ times the energy conversion efficiency compared to the "31" mode harvesters [62].

- Instead of using a single bulk piece of piezoelectric material, the stack is composed of many piezoelectric layers polarized in the "33" direction. Each layer is sandwiched between two electrode layers. This arrangement provides an equivalent piezoelectric constant $\overline{d}_{33}$ as much as the original piezoelectric constant multiplied by the number of layers in the stack.

1.3 ADVANCED PEH CONCEPTS

Since PEHs were first invented, scientists and researchers have been coming up with new ideas and innovations that improve energy efficiency, increase the amount of harvested energy from a source, and invented new energy harvesters. Xu et al. [91, 92, 93] invented many advanced PEH devices, name Hybrid Piezoelectric Harvesting Transducer (HYPEHT). The HYPEHT proved to be significantly better than a same sized cymbal harvester. In addition, it received the 2011 Best Energy Harvesting Technology development award. However, the performance of the invention has not been released yet due to intellectual property issues.

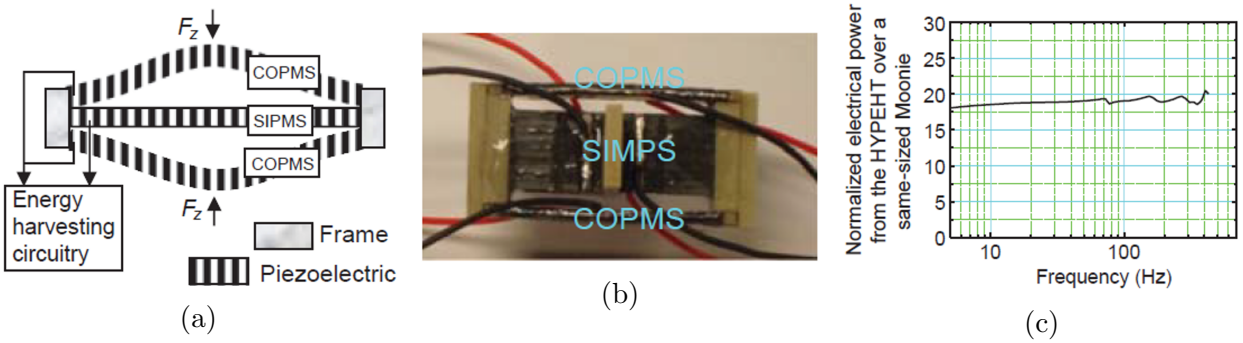

Fig. 7: (a) Diagram of the HYPEHT, (b) Picture of the first prototype HYPEHT (size $35.5 \times 18 \times 10$ mm, weight 40 g) and (c) The harvested power of the HYPEHT over a Moonie-type piezoelectric harvester [62].

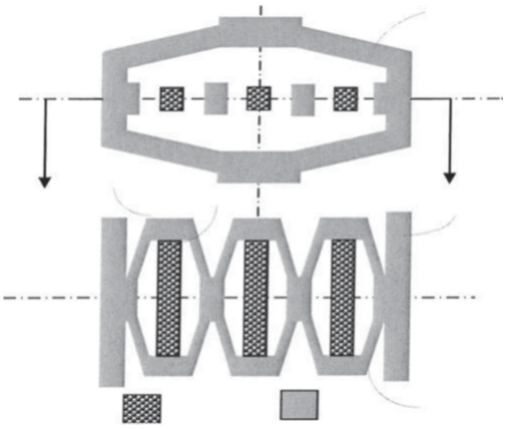

Fig. 8: Multistage Force Amplification Piezoelectric Harvester Transducer (MFAPEHT) [94]

Xu et al. [94] also invented a multistage force amplification piezoelectric harvester transducer (MFAPEHT) (Fig.8). This harvester has three stack. Each stack is mounted in a separate force amplification frame (FAF), and all the frames are assembled inside one big

frame. This arrangement offers huge magnification of the external force and produces a large effective piezoelectric charge constant as follows

$$\sum M = M_1 M_2 M_3 ... M_n \tag{4}$$

$$\overline{d_{33}} = \sum M q p d_{33} \tag{5}$$

They also suggested the implementation of Relaxor piezoelectric single crystal multilayer stacks for energy harvesting transducers (RPSEHT) to the MFAPEHT. As discussed earlier in this thesis PMN-PT and PZN-PT relaxors have higher piezoelectric constants ($d_{33} > 1500pC/N$) and E-M coupling factors ($k_{33} > 0.88$), and they are also suitable in cryogenic applications.

1.4 PURPOSE

In the past decades many numerical and analytical approaches were developed. However, none of the published work targeted comparing these approaches to get a quantitative measure of the difference in accuracy between these models. In the current work, four of the models were used to model piezoelectric multilayer stacks in off resonance mode. These addressed models are

- Quasi-Static Model,
- Single Degree of Freedom Model (SDOF),
- Finite Element Analysis (FEA),
- A Distributed Parameter Model.

Secondly, a FEA model (using ANSYS) and an experimental setup were developed. The ANSYS model simulates the Flextensional Piezoelectric Energy Harvesters (FPEHs) in the resonance mode. Accordingly, a modal and a harmonic modules were used. The ANSYS model results were validated using mesh dependence. while the experiment results were used to validate the ANSYS model results.

This thesis is divided into 6 chapters. Chapter (1) gives a brief preview of the piezoelectric materials from the time quartz was discovered until the discovery of relaxors a few decades ago. In chapter (2) a detailed derivation for the piezoelectric constitutive laws conducted. Both linear and non-linear governing equations are derived. Chapter (3) focuses

on mathematical approaches. The chapter starts with an explanation of the quasi-static model, then the SDOF model and finally describes the ANSYS model (APDL). Chapter (4) focuses on the variational approach used to derive the equation of motion of the piezoelectric multilayer stacks. A comprehensive derivation for the voltage equation is available in that chapter. Chapter (5) explains the experimental setup for the resonance mode testing. Finally, chapter (6) presents the results of the resonance and off-resonance mode models, which includes the three mathematical models, the analytical model, and the experimental results.

CHAPTER 2

CONSTITUTIVE LAWS

Since the 2000s, various attempts and contributions performed to maximize the harvested energy as well as the energy conversion efficiency and practicality of the Piezoelectric Energy Harvesters (PEH). The prefix of piezoelectric came from the Greek word piezein which means press or squeeze, a piezoelectric material is a material that produces electric charge when a stress/force is applied on it and vice versa. This material property was firstly discovered in 1880 by Paul-Jacques Curie in quartz ceramic [44].

2.1 THEORETICAL FORMULATION

The constitutive equations for piezoelectric continuum were first formulated by the IEEE Transactions on Ultrasonics, Ferroelectrics and Frequency Control Society in 1966 and were further revised in 1987 [95]. The governing equation can be described in the index notation form as follows:

$$\varepsilon_{ij} = s^E_{ijkl}\sigma_{kl} + d_{kij}E_k \tag{6}$$

$$D_i = d^E_{ikl}\sigma_{kl} + \epsilon^\sigma_{ik}E_k \tag{7}$$

where ε is the strain tensor , s^E is the elastic compliance at constant electric field, σ is the stress tensor, d is the piezoelectric constants tensor, E is the electric field tensor, D is the electric displacement tensor, ϵ^σ_{ij} is the permittivity measured at constant stress and i, j, k & l can take the values 1, 2 & 3. where the compliance is a 4^{th} rank tensor.

Due to the symmetry of the stress and strain tensors, the notation can be compressed by eliminating the redundant terms [96] by representing the stress and the strain with single

column vectors and Eqs. (6) and (7) can be written as follows

$$\varepsilon_i = s_{ij}^E T_j + d_{ki} E_k \tag{8}$$

$$D_i = d_{ij}^E \sigma_j + \epsilon_{ik}^\sigma E_k. \tag{9}$$

The problem with Eqs. (8) and (9) is that they treat the piezoelectric continuum as a linear medium. Also, they assume pure energy conservation. The first equation describes the mechanical response while the second describes the electrical response. Also, they fail to account for the non-linearity that exists in the piezoelectric materials, and these equations ignore the energy dissipation/damping inside the material [96] whether it is due to elastic hysteresis [97] or electrical hysteresis [98].

Many attempts were made to account for the piezoelectric ceramics non-linearity. Joshi [99] drove the linear constitutive equations for piezoceramics then he extended his work in 1991 [100] and drove constitutive laws that accounts for some important non-linearity in piezoceramics including the non-linear elastic compliance, non-linear dielectric permittivity, etc.

In a piezoelectric device bounded by a control volume, the electric fields and mechanical stresses will vary within that control volume and are governed by:

1. The mechanical equilibrium;
2. Strain compatibility equations;
3. Guass' law, which relates the electric field with the distribution of electric charges;
4. Conservation of charge, electric charges cannot be created nor destroyed;
5. Maxwell's law, the electric field must be curl-free under quasi-static conditions.

2.2 LINEAR CONSTITUTIVE EQUATIONS DERIVATION

There are many derivations that can be found in the literature; however, the following derivations are based on the work done by Joshi [100]. We begin with the equation of the 1^{st} law of thermodynamics

$$\Delta U = Q + W \tag{10}$$

where ΔU is the change in internal energy of a closed system, Q is the heat added and W is the net work done on the system "$-W$". Work can be done either by applying mechanical force or by applying an electric current to the piezoelectric material.

We also need to define the enthalpy as $H = U + pV$, where p and V are the pressure and volumes respectively, so we can write the enthalpy in the form

$$H = U - \sigma_{ij}\varepsilon_{ij} - E_i D_i \tag{11}$$

and its total derivative in the form

$$dH = TdS - \varepsilon_{ij} d\sigma_{ij} - D_i dE_i. \tag{12}$$

Employing the thermodynamic *Gibbs Potential* to derive constitutive equations which states

$$G(p, T) = H - TS \tag{13}$$

where G is Gibbs free potential, H is the the enthalpy, T is the temperature and S is the entropy.

$$G(p,T) = U + pV - TS \tag{14}$$

where U is the internal energy, p is the pressure and V is the volume. Since the only work done on the system (control volume)is by a mechanical stress or electric field, we can write Gibbs law as well as its total differential in the following forms

$$G = U - \sigma_{ij}\varepsilon_{ij} - E_i D_i - TS \tag{15}$$

$$dG = -\varepsilon_{ij} d\sigma_{ij} - D_i dE_i - SdT. \tag{16}$$

We have $G = G(\sigma, E, T)$, and we can expanding the total derivative of G using Tailor series in term

$$dG = \left(\frac{\partial G}{\partial \sigma_{ij}}\right)_{E,T} d\sigma_{ij} + \left(\frac{\partial G}{\partial E_k}\right)_{\sigma,T} dE_k + \left(\frac{\partial G}{\partial T}\right)_{\sigma,E} dT. \tag{17}$$

Nothing that, we ignored the higher order terms. The subscripts mean that the propriety of interest is measured when the subscripted properties were constant. Similarly, we can make the same expansion for ε_{ij}, D_k and S

$$d\varepsilon_{ij} = \left(\frac{\partial \varepsilon_{ij}}{\partial \sigma_{km}}\right)_{E,T} d\sigma_{km} + \left(\frac{\partial \varepsilon_{ij}}{\partial E_k}\right)_{\sigma,T} dE_k + \left(\frac{\partial \varepsilon_{ij}}{\partial T}\right)_{\sigma,E} dT \tag{18}$$

$$dD_k = \left(\frac{\partial D_k}{\partial \sigma_{ij}}\right)_{E,T} d\sigma_{ij} + \left(\frac{\partial D_k}{\partial E_s}\right)_{\sigma,T} dE_s + \left(\frac{\partial D_k}{\partial T}\right)_{\sigma,E} dT \tag{19}$$

$$dS = \left(\frac{\partial S}{\partial \sigma_{ij}}\right)_{E,T} d\sigma_{ij} + \left(\frac{\partial S}{\partial E_s}\right)_{\sigma,T} dE_s + \left(\frac{\partial S}{\partial T}\right)_{\sigma,E} dT. \tag{20}$$

Comparing the expressions in Eqs. (16) and (17) (expression by expression) we can reach

the following conclusion

$$\varepsilon_{ij} = -\left(\frac{\partial G}{\partial \sigma_{ij}}\right)_{E,T}$$
$$D_k = -\left(\frac{\partial G}{\partial E_k}\right)_{\sigma,T}$$
$$S = \left(\frac{\partial G}{\partial T}\right)_{\sigma,E}.$$

The generalized Hook's law at constant temperature and electric field can be written as

$$s_{ijkm}^{E,T} = \left(\frac{\partial \varepsilon_{ij}}{\partial \sigma_{km}}\right)_{E,T}. \tag{21}$$

Uchino [101] defined the strain caused by thermal energy or mechanical stress as thermal expansion and elastic deformation respectively. He then defined the strain caused by an electric field as *electric-field induced strain* which is described as *electrostrition*. A third rank tensor is exemplified by piezoelectric charge constants d_{ijk}. For the direct piezoelectric effect its the polarization generated per unit applied stress. For the converse piezoelectric effect, providing a relation of the induced strain ε_{ij} with the applied electric field E_i (V/m), or in the case of direct piezoelectric effect, the induced electric field D_k with the mechanical stress applied on the material σ_{ij} is

$$d_{ijk}^{T} = \left(\frac{\partial \varepsilon_{ij}}{\partial E_k}\right)_{\sigma,T} \tag{22}$$
$$= \left(\frac{\partial D_k}{\partial \sigma_{ij}}\right)_{E,T}. \tag{23}$$

Thermal expansion "α" is a second rank tensor that is defined as the tendency of the material to change its shape or geometry or undergo strain as a response of the change in temperature [102]. Also, it relates the stress tensor with the entropy of the material

[103, 104]

$$\alpha_{ij}^{E} = \left(\frac{\partial \varepsilon_{ij}}{\partial T}\right)_{\sigma,E} \tag{24}$$

$$= \left(\frac{\partial S}{\partial \sigma_{ij}}\right)_{E,T}. \tag{25}$$

The dielectric permittivity ϵ_{ij} also known as the dielectric constant is defined as the dielectric displacement D_i per unit electric field E_j [105].

$$\epsilon_{ij}^{\sigma,T} = \left(\frac{\partial D_i}{\partial E_j}\right)_{\sigma,T}. \tag{26}$$

Some materials are known as polar or pyroelectric material, Pyr in Greek means fire. The coefficient of pyroelectricity is defined as [106]

$$p_i^{\sigma} = \left(\frac{\partial D_i}{\partial T}\right)_{\sigma,E} \tag{27}$$

$$= \left(\frac{\partial S}{\partial E_i}\right)_{\sigma,T}. \tag{28}$$

the specific heat is also defined as

$$c^{\sigma,E} = \frac{T_0}{\rho}\left(\frac{\partial S}{\partial T}\right)_{\sigma,E} \tag{29}$$

$$\frac{\rho c^{\sigma,E}}{T_0} = \left(\frac{\partial S}{\partial T}\right)_{\sigma,E}. \tag{30}$$

Now, we can start assembling Eqs. (21), (23) and (24) into Eq.(18), and we get

$$d\varepsilon_{ij} = s^{E,T}_{ijkm} d\sigma_{km} + d^{T}_{ijk} dE_k + \alpha^{E}_{ij} dT \tag{31}$$

Assembling Eqs. (23), (26) and (27) into Eq.(19) we get

$$dD_k = d^{T}_{ijk} d\sigma_{ij} + \epsilon^{\sigma,T}_{ij} dE_j + p^{\sigma}_{i} dT. \tag{32}$$

Similarly, with Eq. (25), (28) and (30) into Eq. (20)

$$dS = \alpha^{E}_{ij} d\sigma_{ij} + p^{\sigma}_{i} dE_i + \frac{\rho c^{\sigma,E}}{T_0} dT. \tag{33}$$

Integrating Eqs. (31), (32) and (33) we get

$$\varepsilon_{ij} = s^{E,T}_{ijkm} \sigma_{km} + d^{T}_{ijk} E_k + \alpha^{E}_{ij} T \tag{34}$$

$$D_i = d^{T}_{ijk} \sigma_{ij} + \epsilon^{\sigma,T}_{ij} E_j + p^{\sigma}_{i} \Delta T \tag{35}$$

$$\Delta S = \alpha^{E}_{ij} \sigma_{ij} + p^{\sigma}_{i} E_i + \frac{\rho c^{\sigma,E}}{T_0} \Delta T. \tag{36}$$

The constitutive equations above are for a general piezoelectric ceramic. In an isothermal system (T = constant) will lead us to the required Eqs. (6) and (7)

$$\varepsilon_{ij} = s^{E,T}_{ijkm} \sigma_{km} + d^{T}_{ijk} E_k \tag{6}$$

$$D_i = d^{T}_{ijk} \sigma_{ij} + \epsilon^{\sigma,T}_{ij} E_j. \tag{7}$$

2.3 NON-LINEAR CONSTITUTIVE EQUATIONS DERIVATION

In the previous section, we viewed the derivation process of the linear piezoelectric constitutive laws. Fig.(9) shows a typical hysteresis curve made by utilizing the converse piezoelectric effect, i.e, applying electric field until reaching the maximum strain then removing or reversing the electric field. Fig.(9a) when applying an electric field, a change in strain occurs (branch A); however, when we remove that electric field the strain does not follow path A and follows path B instead. In addition to the normal hysteresis curves A and B in Fig.(9a), when the applied voltage is positive, the butterfly diagram in Fig.(9b) defines the behavior of the material through AC field cycles of positive and negative operating electric fields. Negative electric fields produce negative strain along curve C until the depoling field where the extension suddenly turns positive following the curve D. The process is repeated along curves EFG when the electric field is made positive again. The "butterfly" diagram provides a complete characterization of the depoling and repoling process. More information on the hysteresis curve of polymerization can be found in [107].

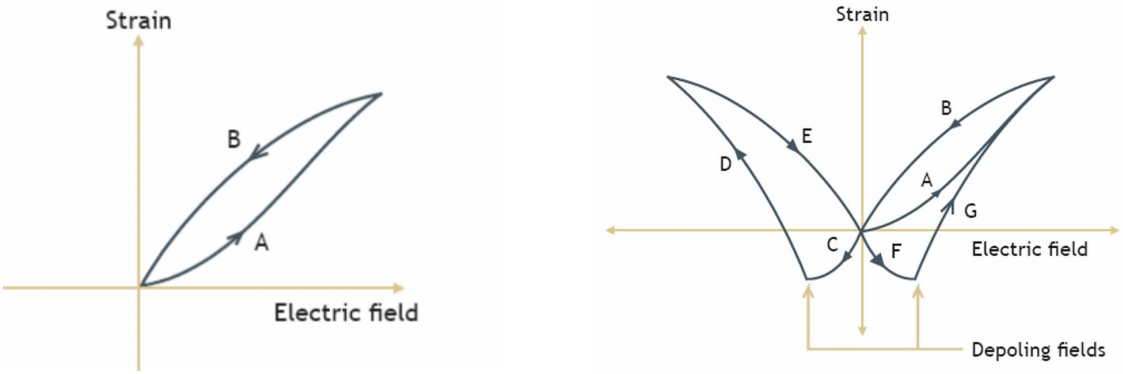

(a) Applied DC voltage to a piezoelectric ceramic (b) Applied AC voltage to a piezoelectric ceramic

Fig. 9: Piezoelectric ceramic hysteresis behavior [108]

In the derivation in the previous section we neglected the higher order terms in Eqs.(18),

(19) and (20) which resulted in the linear constitutive equations. In our non-linear derivations we will consider the second-order terms. We start by re-writing Eq.(18) to get the following formula

$$d\varepsilon_{ij} = \left(\frac{\partial \varepsilon_{ij}}{\partial \sigma_{km}}\right)_{E,T} d\sigma_{km} + \left(\frac{\partial \varepsilon_{ij}}{\partial E_k}\right)_{\sigma,T} dE_k + \left(\frac{\partial \varepsilon_{ij}}{\partial T}\right)_{\sigma,E} dT + \frac{1}{2}\left(\frac{\partial^2 \varepsilon_{ij}}{\partial \sigma_{sm}\partial \sigma_{pq}}\right)_{E,T} d\sigma_{sm} d\sigma_{pq} + \frac{1}{2}\left(\frac{\partial^2 \varepsilon_{ij}}{\partial E_n \partial E_r}\right)_{\sigma,T} dE_n dE_r + \frac{1}{2}\left(\frac{\partial^2 \varepsilon_{ij}}{\partial T^2}\right)_{\sigma,E} dT dT + \left(\frac{\partial^2 \varepsilon_{ij}}{\partial \sigma_{sm}\partial E_r}\right)_{T} d\sigma_{sm} dE_r + \left(\frac{\partial^2 \varepsilon_{ij}}{\partial \sigma_{pm}\partial T}\right)_{E} d\sigma_{pm} dT + \left(\frac{\partial^2 \varepsilon_{ij}}{\partial E_n \partial T}\right)_{\sigma} dE_n dT. \quad (37)$$

Similarly Eq.(19) can be written as

$$dD_k = \left(\frac{\partial D_k}{\partial \sigma_{im}}\right)_{E,T} d\sigma_{im} + \left(\frac{\partial D_k}{\partial E_n}\right)_{\sigma,T} dE_n + \left(\frac{\partial D_k}{\partial T}\right)_{\sigma,E} dT + \frac{1}{2}\left(\frac{\partial^2 D_k}{\partial \sigma_{im}\partial \sigma_{pq}}\right)_{E,T} d\sigma_{im} d\sigma_{pq} + \frac{1}{2}\left(\frac{\partial^2 D_k}{\partial E_n \partial E_r}\right)_{\sigma,T} dE_n dE_r + \frac{1}{2}\left(\frac{\partial^2 D_k}{\partial T^2}\right)_{\sigma,E} dT dT + \left(\frac{\partial^2 D_k}{\partial \sigma_{im}\partial E_n}\right)_{T} d\sigma_{im} dE_n + \left(\frac{\partial^2 D_k}{\partial \sigma_{im}\partial T}\right)_{E} d\sigma_{im} dT + \left(\frac{\partial^2 D_k}{\partial E_m \partial T}\right)_{\sigma} dE_m dT. \quad (38)$$

Also, for Eq.(20):

$$dS = \left(\frac{\partial S}{\partial \sigma_{im}}\right)_{E,T} d\sigma_{im} + \left(\frac{\partial D_k}{\partial E_n}\right)_{\sigma,T} dE_n + \left(\frac{\partial S}{\partial T}\right)_{\sigma,E} dT + \frac{1}{2}\left(\frac{\partial^2 S}{\partial \sigma_{im}\partial \sigma_{pq}}\right)_{E,T} d\sigma_{im} d\sigma_{pq} + \frac{1}{2}\left(\frac{\partial^2 S}{\partial E_n \partial E_r}\right)_{\sigma,T} dE_n dE_r + \frac{1}{2}\left(\frac{\partial^2 S}{\partial T^2}\right)_{\sigma,E} dT dT + \left(\frac{\partial^2 S}{\partial \sigma_{im}\partial E_n}\right)_{T} d\sigma_{im} dE_n + \left(\frac{\partial^2 S}{\partial \sigma_{im}\partial T}\right)_{E} d\sigma_{im} dT + \left(\frac{\partial^2 S}{\partial E_m \partial T}\right)_{\sigma} dE_m dT. \quad (39)$$

If we assumed negligible change in temperature the three previous equations become

$$d\varepsilon_{ij} = \left(\frac{\partial \varepsilon_{ij}}{\partial \sigma_{km}}\right)_E d\sigma_{km} + \left(\frac{\partial \varepsilon_{ij}}{\partial E_k}\right)_\sigma dE_k + \frac{1}{2}\Bigg(\left(\frac{\partial^2 \varepsilon_{ij}}{\partial \sigma_{im}\partial \sigma_{pq}}\right)_E d\sigma_{im} d\sigma_{pq} + \left(\frac{\partial^2 \varepsilon_{ij}}{\partial E_n \partial E_r}\right)_\sigma dE_n dE_r \Bigg) + \left(\frac{\partial^2 \varepsilon_{ij}}{\partial \sigma_{sm}\partial E_r}\right)_T d\sigma_{sm} dE_r. \quad (40)$$

$$dD_k = \left(\frac{\partial D_k}{\partial \sigma_{im}}\right)_E d\sigma_{im} + \left(\frac{\partial D_k}{\partial E_n}\right)_\sigma dE_n + \frac{1}{2}\Bigg(\left(\frac{\partial^2 D_k}{\partial \sigma_{im}\partial \sigma_{pq}}\right)_E d\sigma_{im} d\sigma_{pq} + \left(\frac{\partial^2 D_k}{\partial E_n \partial E_r}\right)_\sigma dE_n dE_r \Bigg) + \left(\frac{\partial^2 D_k}{\partial \sigma_{im}\partial E_n}\right)_T d\sigma_{im} dE_n. \quad (41)$$

We have the non-linear compliance coefficient

$$S^E_{ijkmpq} = \left(\frac{\partial^2 \varepsilon_{ij}}{\partial \sigma_{km}\partial \sigma_{pq}}\right)_E. \quad (42)$$

The non-linear piezoelectric charge constants

$$d^T_{ijnr} = \left(\frac{\partial^2 \varepsilon_{ij}}{\partial E_n \partial E_r}\right)_\sigma \quad (43)$$

$$= \left(\frac{\partial^2 D_k}{\partial \sigma_{lm}\partial E_n}\right)_T d\sigma_{lm} dE_n. \quad (44)$$

The non-linear elastostriction coefficients

$$\kappa_{ijlmn} = \left(\frac{\partial^2 \varepsilon_{ij}}{\partial \sigma_{im}\partial E_n}\right) \quad (45)$$

$$= \left(\frac{\partial^2 D_k}{\partial \sigma_{lm}\partial \sigma_{pq}}\right)_E. \quad (46)$$

And finally the non-linear dielectric permittivity

$$\epsilon_{knr} = \left(\frac{\partial^2 D_k}{\partial E_n \partial E_r} \right). \tag{47}$$

Therefore, the differential governing equation becomes

$$d\varepsilon_{ij} = s^E_{ijkm} d\sigma_{km} + d_{ijk} dE_k + \frac{1}{2} S^E_{ijkmpq} d\sigma_{km} d\sigma_{pq} + \frac{1}{2} d_{ijnr} dE_n dE_r + \kappa_{ijlmn} d\sigma_{lm} dE_n \tag{48}$$

$$dD_i = d_{ijk} d\sigma_{jk} + \epsilon_{in} dE_n + \frac{1}{2} \kappa_{ijlmn} d\sigma_{jl} d\sigma_{mn} + \frac{1}{2} \epsilon^{\sigma}_{inr} dE_n dE_r + d_{ilmn} d\sigma_{lm} dE_n. \tag{49}$$

By integration we finally reach the non-linear governing equations

$$\varepsilon_{ij} = s^E_{ijkm} \sigma_{km} + d_{ijk} E_k + \frac{1}{2} S^E_{ijkmpq} \sigma_{km} \sigma_{pq} + \frac{1}{2} d_{ijnr} E_n E_r + \kappa_{ijlmn} \sigma_{lm} E_n \tag{50}$$

$$D_i = d_{ijk} \sigma_{jk} + \epsilon_{in} E_n + \frac{1}{2} \kappa_{ijlmn} \sigma_{jl} \sigma_{mn} + \frac{1}{2} \epsilon^{\sigma}_{inr} E_n E_r + d_{ilmn} \sigma_{lm} E_n. \tag{51}$$

Ceramics are brittle materials, and so as piezoelectric ceramics, they fail in tension at relatively low values of strain. The stress-strain curve is linear up to failure (parabolic in other cases); therefore, the non-linear compliance can be neglected, and we can also neglect the non-linear dielectric constant

The elastostriction coefficients κ_{ijlmn} are important at high electric fields. If mechanical stress and electric field are applied together (the material is not allowed to deform freely).

By making use of the symmetry of the stress and the strain tensors as in the previous section we get the final form of the non-linear constitutive laws:

$$\varepsilon_i = s^E_{ij} \sigma_j + d_{ik} E_k + \frac{1}{2} d^E_{ikm} E_k E_m + \kappa_{imn} \sigma_m E_n \tag{52}$$

$$D_i = d_{ij} \sigma_j + \epsilon^{\sigma}_{in} E_n + \frac{1}{2} \kappa_{ijl} \sigma_j \sigma_l + d_{ilm} \sigma_l E_m. \tag{53}$$

2.4 CASE STUDY

We have the linear compliance coefficients tensor expressed as follows

$$s_{ijkm} = \begin{bmatrix} s_{1111} & s_{1122} & s_{1133} & s_{1123} & s_{1113} & s_{1112} \\ & s_{2222} & s_{2233} & s_{2223} & s_{2213} & s_{2212} \\ & & s_{3333} & s_{3323} & s_{3313} & s_{3312} \\ & \text{sym.} & & s_{2323} & s_{2313} & s_{2312} \\ & & & & s_{1313} & s_{1312} \\ & & & & & s_{1212} \end{bmatrix}. \tag{54}$$

The piezoelectric multilayer stack (shown in Fig. (10)) can be treated as a *transversely isotropic solids/composite materials*. A transversely isotropic solid is a material that has an axis of symmetry. Suppose that we have the axis of symmetry as the x_3-axis in the Cartesian coordinates. We start by noting that the material is also symmetric about the x_1 and x_2 planes. Starting with applying the symmetry around x_1 by employing the improper orthogonal transformation [1] Q_{ij} (the following derivation is from R.Ash [109])

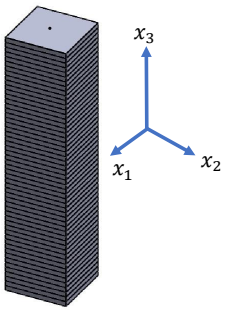

Fig. 10: Piezoelectric multi-layer Stack

[1] Improper means that the transformation results in a non-right hand coordinate system

$$Q_{ij} = \begin{bmatrix} -1 & 0 & 0 \\ 0 & 1 & 0 \\ 0 & 0 & 1 \end{bmatrix} \tag{55}$$

The fourth order tensor transformation follows the following equation.

$$s'_{ijkm} = Q_{im}Q_{jn}Q_{kp}Q_{mq}s_{mnpq} \tag{56}$$

Upon proceeding in the transformation, we will notice that any element involving any odd number of subscripts 1 repetitions will yield the improper transformation, accordingly:

$$s_{1113} = s_{1112} = s_{2213} = s_{2212} = s_{3313} = s_{2313} = s_{2312} = 0.$$

$$\therefore s^1_{ijkm} = \begin{bmatrix} s_{1111} & s_{1122} & s_{1133} & s_{1123} & 0 & 0 \\ & s_{2222} & s_{2233} & s_{2223} & 0 & 0 \\ & & s_{3333} & s_{3323} & 0 & 0 \\ & \text{sym.} & & s_{2323} & 0 & 0 \\ & & & & s_{1313} & s_{1312} \\ & & & & & s_{1212} \end{bmatrix}. \tag{57}$$

Similarly, for the symmetry around the x_2 plan we employ the following transformation matrix

$$Q_{ij} = \begin{bmatrix} 1 & 0 & 0 \\ 0 & -1 & 0 \\ 0 & 0 & 1 \end{bmatrix}. \tag{58}$$

Then we gave also s_{1312}, s_{3323}, s_{1123} and $s_{2223} = 0$.

$$\therefore s_{ijkm}^{1-2} = \begin{bmatrix} s_{1111} & s_{1122} & s_{1133} & 0 & 0 & 0 \\ & s_{2222} & s_{2233} & 0 & 0 & 0 \\ & & s_{3333} & 0 & 0 & 0 \\ & \text{sym.} & & s_{2323} & 0 & 0 \\ & & & & s_{1313} & 0 \\ & & & & & s_{1212} \end{bmatrix} \tag{59}$$

We have symmetry about the x_3 axis by applying the following transformation matrix

$$Q_{ij} = \begin{bmatrix} cos\theta & sin\theta & 0 \\ -sin\theta & sin\theta & 0 \\ 0 & 0 & 1 \end{bmatrix} \tag{60}$$

and substituting in $S'_{ijkm} = Q_{im}Q_{jn}Q_{kp}Q_{mq}S_{mnpq}$ to get the following sets of equations

$$
\begin{aligned}
s_{1111} &= cos^4\theta.s_{1111} + cos^2\theta.sin^2\theta[2s_{1122} + 4s_{1212}] + sin^4\theta.s_{2222} \\
s_{2222} &= sin^4\theta.s_{1111} + cos^2\theta.sin^2\theta[2s_{1122} + 4s_{1212}] + cos^4\theta.s_{2222} \\
s_{1122} &= cos^4\theta.s_{1122} + sin^4\theta.s_{2211} + cos^2\theta.sin^2\theta[s_{1111} + s_{2222}] - 4s_{1212} \\
s_{1133} &= cos^2\theta.s_{1133} + sin^2\theta.s_{2233} \\
s_{1212} &= (cos^4\theta + sin^4\theta)s_{1212} + cos^2\theta.sin^2\theta[s_{1111} - 2s_{1122} - 2s_{1212} + s_{2222}].
\end{aligned}
$$

The equations above must be true for all values of θ. By investigating and substituting these equations together we can reach the following conclusion.

$$
\begin{aligned}
s_{1111} &= s_{2222} \\
s_{1133} &= s_{2233} \\
s_{2323} &= s_{3131} \\
s_{1212} &= \frac{1}{2}(s_{1111} - s_{1122})
\end{aligned}
$$

Accordingly, we can write the compliance matrix in the following form

$$
\therefore s_{ijkm} = \begin{bmatrix}
s_{1111} & s_{1122} & s_{1133} & 0 & 0 & 0 \\
 & s_{1111} & s_{2233} & 0 & 0 & 0 \\
 & & s_{3333} & 0 & 0 & 0 \\
 & \text{sym.} & & s_{2323} & 0 & 0 \\
 & & & & s_{2323} & 0 \\
 & & & & & \frac{1}{2}(s_{1111} - s_{1122})
\end{bmatrix} \tag{61}
$$

$$\therefore s_{ij} = \begin{bmatrix} s_{11} & s_{12} & s_{13} & 0 & 0 & 0 \\ & s_{11} & s_{13} & 0 & 0 & 0 \\ & & s_{33} & 0 & 0 & 0 \\ & \text{sym.} & & s_{44} & 0 & 0 \\ & & & & s_{44} & 0 \\ & & & & & \frac{1}{2}(s_{11} - s_{12}) \end{bmatrix}. \tag{62}$$

Using similar methods, we can derive the tensors for the d_{ijk} and ϵ_{ij} which is an orthographic type matrix.

CHAPTER 3

MATHEMATICAL METHODOLOGIES

In this chapter, we will present a detailed explanation of the mathematical approaches and experimental setup used in the current work. We will first discuss the Static Model, then the SDOF model, then the Finite Element Model. This progression in explanation by disgusting the simplest model to the more difficult ones will allow the reader to the piezoelectric stack numerical simulations.

These numerical models adopt the assumption that the force affects the piezoelectric stack in only the "33" direction, and the piezoelectric effect in the other directions will be ignored. Accordingly, Eqs. (6) and (7) can be reduced as follows.

$$\varepsilon_3 = s_{33}^E \sigma_3 + d_{33} E_3 \tag{63}$$

$$D_3 = d_{33}^E \sigma_3 + \epsilon_{33}^\sigma E_3 \tag{64}$$

3.1 QUASI-STATIC MODEL

The static model was presented in many papers and textbooks in the literature. In this work we will be focusing on the model presented by Uchino [101]. Further modifications to this model were made by Xu et al. [69], but we will not delve to these modifications in the current work.

The stress is expressed as the ratio between the input force and the normal area as follows

$$\sigma_3(t) = \frac{F(t)}{A}. \tag{65}$$

Using this calculated stress, we can calculate the dielectric displacement using Eq. (66).

$$D_3(t) = d_{33}\sigma_3(t) \tag{66}$$

The next step will be to calculate the Electric Field Vector by substituting into Eq. (67).

$$E_3(t) = \frac{D_3(t)}{\epsilon_{33}^{\sigma(t)}} \tag{67}$$

Finally, the applied voltage is calculated using the following equation

$$V(t) = E_3(t)t_p. \tag{68}$$

If we assumed a sinusoidal input force on the piezoelectric stack, the derivative of the voltage with respect to time can be expressed as

$$\frac{dV(t)}{dt} = \frac{2\pi f t_p d_{33} Amp}{A\epsilon_{33}^{\sigma}} cos(2\pi f t). \tag{69}$$

Accordingly, the open circuit current can be calculated as

$$i(t) = \frac{dV(t)}{dt} C_p \tag{70}$$

where C_P is the stack capacitance

$$C_p = \frac{pA\epsilon_{33}^{T}}{t_p}, \tag{71}$$

and the Generated Energy can be calculated using Eq. (72)

$$En(t) = \frac{1}{2} C_p V^2(t). \tag{72}$$

3.2 SINGLE DEGREE OF FREEDOM MODEL (SDOF)

The main physical difference between the Static model and the Single Degree of freedom model is that the SDOF model accounts for the inertia effects. The SDOF is relatively simple and provides fairly accurate results [9]. In this thesis we will derive the governing equations for the SDOF model. The SDOF is by far the most implemented model in the literature [79, 110, 75, 70, 94]. The SDOF model was first presented by Goldfarb et al. [111] where the piezoelectric multi-layer stack is modeled as a mass-spring-damper system as shown in Fig. (11a).

The mechanical response of the system to be shown in Fig.(11b) can be written as

$$M\ddot{x} = -F_p(t) + F(t). \tag{73}$$

By convention and similar to the quasi-static model in section 3.1, coordinate transformations are performed so that the 3 direction is aligned with the polarization direction. In case we are modeling a harvester operated in the "33" mode the other directions are ignored as discussed previously, and again we use the following well known equations:

$$S_3 = s_{33}^E T_3 + d_{33} E_3 \tag{63}$$

$$D_3 = d_{33}^E T_3 + \varepsilon_{33}^T E_3 \tag{64}$$

where Eqs. (63) and (64) ignored the piezoelectric and strain effects in the other directions.

The SDOF model used on the following simplified constitutive relations is

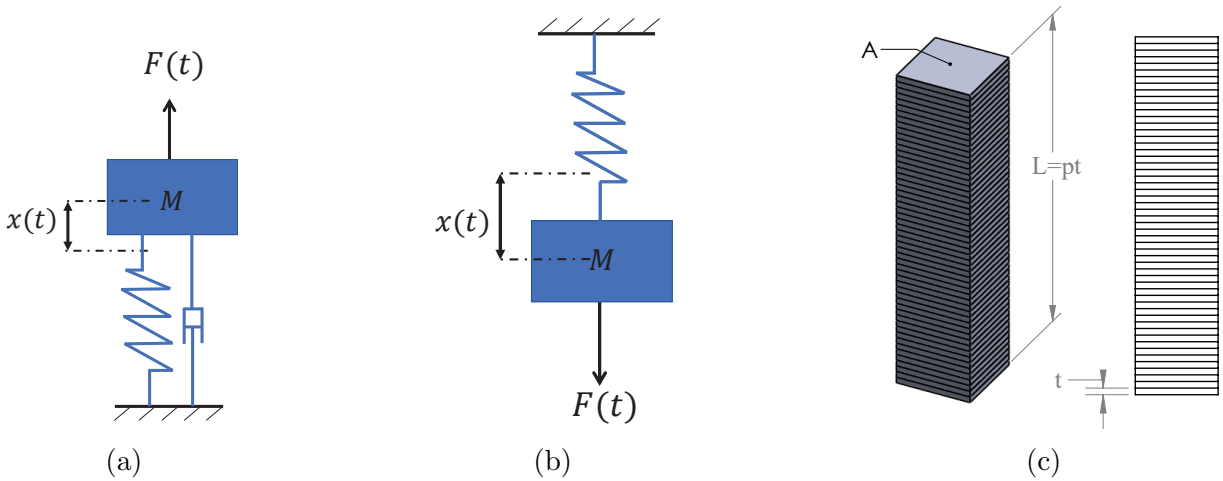

(a) (b) (c)

Fig. 11: Single Degree of Freedom Physical Modeling (a) Mass-Spring System proposed by Feenstra et al. [110] (b) Mass-Spring-Damper model proposed by Glodfard et al. [111] (c) Piezoelectric Stack operating in "33" mode

$$S_3(t) = \frac{x_3}{L} \qquad \sigma_3 = \frac{F(t)}{A} \qquad E_3 = \frac{V(t)}{t_p} \qquad D_3 = \frac{Q_3(t)}{A}.$$

Accordingly, Eqs. (63) and (64) can be expressed as

$$x(t) = \frac{L}{YA}F_p(t) + \frac{d_{33}L}{t_p}V(t) \Rightarrow F_p = \frac{YA}{L}x(t) - \frac{d_{33}YA}{t_pC_p}Q(t) \tag{74}$$

$$Q(t) = d_{33}pF(t) + C_pV(t) \tag{75}$$

where $C_p = \frac{p\varepsilon_{33}^{\sigma}A}{t_p}$ and $k = \frac{YA}{L}$.

By rearranging Eq. (75), we get the following equation.

$$V(t) = \frac{d_{33}pkx(t)}{C_p} + \frac{Q(t)}{C_p} \tag{76}$$

Applying Newton's law on the mass-spring system shown in Fig. 11 we get the following equation

$$M\ddot{x} + F_p(t) = F(t). \tag{77}$$

Accordingly, the mechanical and the electrical responses can be coupled and represented in the following equations which are the basis for the SDOF model.

$$M\ddot{x} + kx(t) - \frac{d_{33}kl}{t_p C_p} Q(t) = F(t) \tag{78}$$

$$R\dot{Q}(t) - \frac{d_{33}pk}{C_p} x(t) + \frac{C_p}{Q(t)} = 0 \tag{79}$$

Although the single degree of freedom model is very simple and provides good accuracy, it assumes that the system is following linear behavior. Also, it assumes that the PZT stack is homogeneous across all the layers, i.e. the generated voltage and current through out all the layers is identical "$L = pt$". Also SDOF can not produce a whole bode plot diagram; instead it produces only one peak on it [70, 112].

Among the limitations in Eqs. (78) and (79) is that they assume the piezoelectric continuum to be linear and also they assume that the process of energy conversion has 100% efficiency. Eq. (78) governs the mechanical response of the system while Eq. (79) governs the electrical resonance; hence, it fails to account for the non-linearity that exists in the piezoelectric stack. Also, these equations ignore the energy dissipation/damping inside the material whether it is due to elastic hysteresis [97] or electrical hysteresis [98] as well as the presence of electrodes between the stack layers.

Many attempts were made to account for the piezoelectric ceramics non-linearity [113, 114, 115, 116]. Leigh et al. [117] proposed an implicit iterative approach that predicted the hysteresis in the piezoelectric actuators; however, due to the iterative approach any noise in the input will be magnified [118]. Also, this approach is not a real-time approach, and it is not an energy based approach [111].

If we substituted with the natural frequency $\omega_n = \sqrt{\frac{YA}{ML}}$, Eqs. (78) and (79) can be rewritten in the following forms

$$\ddot{x}(t) + \omega_n^2 x(t) - p\omega_n^2 d_{33} V(t) = \frac{\alpha}{M} F(t) \tag{80}$$

$$Q_3(t) + p d_{33} M \omega_n^2 x(t) + C_p V(t). \tag{81}$$

Knowing that the voltage can be expressed as $V(t) = \frac{R}{\dot{Q}(t)}$, Eq. (81) can be rewritten as follows

$$\dot{V}(t) + \frac{V(t)}{RC_p} + \frac{pM\omega_n^2 d_{33}}{C_p} = 0. \tag{82}$$

Laplace and Fourier transforms can be used to solve Eqs. (80) and (82); however, the transformation of these two equations to the s-domain or the frequency domain will result in very large equations, and the chance of making an error is almost unavoidable (even if the transformation was carried out using software like MATLAB).

An easier way to solve these equations is to use the state space modeling by defining the state variables as follows

$$x_1 = x \tag{83}$$

$$\dot{x_1} = \dot{x} \tag{84}$$

$$x_2 = \dot{x_1} = \dot{x} \tag{85}$$

$$\dot{x_2} = \ddot{x_1} = \ddot{x} \tag{86}$$

$$x_3 = V \tag{87}$$

$$\dot{x_3} = \dot{V}. \tag{88}$$

Substituting the values of the state variables in Eqs. (80) and (82) we get a set of three equations.

$$\dot{x_1} = x_2 \tag{89}$$

$$\dot{x_2}(t) + \omega_n^2 x_1(t) - p\omega_n^2 d_{33} x_3(t) = \frac{\alpha}{M} F(t) \tag{90}$$

$$\dot{x_3}(t) + \frac{x_3(t)}{RC_p} + \frac{pM\omega_n^2 d_{33}}{C_p} = 0 \tag{91}$$

Equations (89), (90) and (91) can be rearranged as expressed as

$$\dot{x_1}(t) = x_2(t) \tag{92}$$

$$\dot{x_2}(t) = -\omega_n^2 x_1(t) + p\omega_n^2 d_{33} x_3(t) + \frac{\alpha}{M} F(t) \tag{93}$$

$$\dot{x_3}(t) = -\frac{x_3(t)}{RC_p} - \frac{pM\omega_n^2 d_{33}}{C_p}. \tag{94}$$

Defining an equivalent piezoelectric constant for the stack assembly as shown in Eq. (95),

$$\overline{d_{33}} = p d_{33}. \tag{95}$$

Substituting Eq. (95) in Eqs (89), (90) and (91) we get

$$\dot{x_1}(t) = x_2(t) \tag{96}$$

$$\dot{x_2}(t) = -\omega_n^2 x_1(t) + \omega_n^2 \overline{d_{33}} x_3(t) + \frac{\alpha}{M} F(t) \tag{97}$$

$$\dot{x_3}(t) = -\frac{x_3(t)}{RC_p} - \frac{M\omega_n^2 \overline{d_{33}}}{C_p}. \tag{98}$$

MATLAB's standard solver for Ordinary Differential Equations (ODE) was used, specifically the ode45. The ode45 utilizes an algorithm that is similar to the Runge-Kutta method with a variable time step which is more efficient in many cases. The solver's initial conditions were set to be zero before starting the solution process.

3.3 FINITE ELEMENT ANALYSIS

Due to the complexity of this method we used the ANSYS APDL to simulate the piezoelectric stack. ANSYS users, have two choices: either use the ANSYS APDL or the ANSYS structural workbench. The APDL stands for ANSYS Parametric Design Language. It is more complicated in terms of drawing the geometry and setting up the mathematical model; however, it gives more control and insight and provides great understanding of the model that is being solved.

On the other hand, the ANSYS workbench has a more friendly GUI (Graphical User Interface). The user can input the parameters and control every aspect in the model the same as the APDL by using the commands options. However, the ANSYS workbench has an ACT called "ANSYS Piezo-Electric and MEMS" that can be downloaded for free from the ANSYS website and added as an extension to the workbench. Using this extension makes the Piezoelectric effect simulations easy even for beginners.

Three ANSYS models were used; static, transient and harmonic models were tested. The first model that was implemented was the static model, then the transient model and finally the harmonic model. The harmonic model is a very tricky model when applying a voltage boundary condition.

The piezoelectric stack by itself was modeled and different harvester's geometries were modeled as well. In this section we will be discussing a whole harvester. Modeling will be presented as the explanation of a piezoelectric stack modeling as part of the whole ANSYS modeling process.

To model the stainless steel (Spring Metal) the FAF is modeled using $3D$ 10 node

tetrahedral Elements SOLID187 (Fig. (12)) which has degrees of freedom limited only to the spatial directions. On the other hand, the piezoelectric stack was modeled using $3D$ 20-Node Coupled-Field Solid SOLID226 Elements (Fig. (13)). These elements have similar geometry as SOLID186 except that they allow voltage as an additional degree of freedom. The stack is modeled as one piezoelectric piece rather than sets of separate layers of piezoelectric and silver electrodes. This allows using bigger mesh elements and significantly reduces computational time.

To apply the SOLID226 to a specific geometry (the piezoelectric stacks), the following command is used "$ET, MATID, SOLID226, 1001$", where MATID is the material identification number, and the number 1001 turns on the keyopt for the volt degree of freedom for SOLID226.

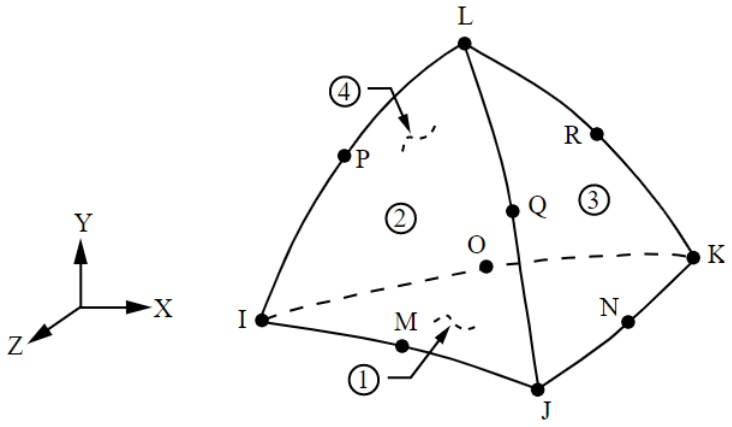

Fig. 12: SOLID186 Homogeneous Structural Solid Geometry

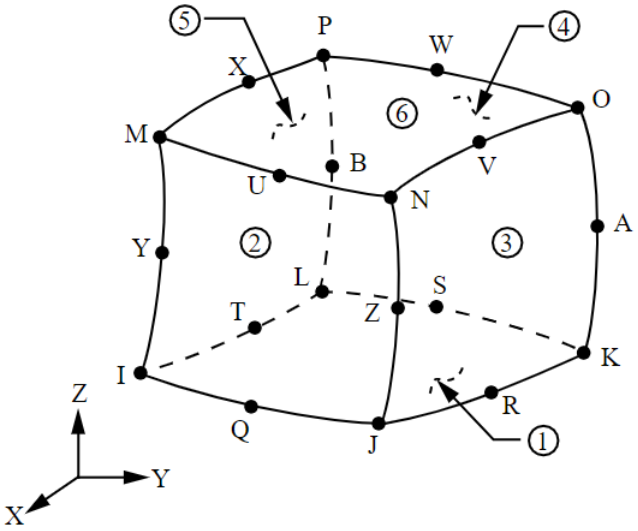

Fig. 13: SOLID226 Element Geometry

After defining the elements types, the material properties are defined. The FAF is defined normally like any other isotropic materials found in the literature.

Although the piezoelectric materials are anisotropic, we can take advantage of the presence of multilayers in the stack, and each layer is very thin (as small as 0.1 mm) and the force is applied only in the "33" direction; therefore, we can neglect the piezoelectric effects in the other directions. Accordingly, for simplicity we can assume that the piezoelectric stack is isotropic.

To treat the piezoelectric multi-layer stack as one bulk object we need to use the material equivalence method which was implemented by Feng et al. [74]. The material equivalence method assumes the following

$$\overline{C_p} = C_p \tag{99}$$

where $\overline{C_p}$ and C_p are the capacitance of the piezoelectric bulk and the capacitance of the multi-layer stack respectively.

The Capacitance of the stack with layers is expressed as

$$C_p = \frac{p\varepsilon_{33}^{\sigma} A}{t_p}. \tag{100}$$

While Capacitance of the piezoelectric bulk is expressed as

$$\overline{C_p} = \frac{\varepsilon_{33}^{\sigma} A}{p t_p} \tag{101}$$

where $L = pt_p$.

From Eqs.(99), (100) and (101) we get

$$\frac{p\varepsilon_{33}^{\sigma} A}{t_p} = \frac{\varepsilon_{33}^{\sigma} A}{p t_p}. \tag{102}$$

Therefore, we get the equivalent dielectric constant as follows

$$\overline{\varepsilon_{33}^{\sigma}} = p^2 \varepsilon_{33}^{\sigma}. \tag{103}$$

Also, it was shown in section (3.2) that the equivalent piezoelectric charge constant is expressed as follows

$$\overline{d_{33}} = p d_{33}.$$

The rest of the piezoelectric parameters can be expressed as

$$\overline{e_{33}} = \frac{\overline{d_{33}}^2}{s_{33}^E} \tag{104}$$

$$\overline{\varepsilon_{33}^{s}} = \overline{\varepsilon_{33}^{\sigma}} - (\frac{\overline{d_{33}}^2}{s_{33}^E}). \tag{105}$$

The main parameters used to model the piezoelectric material are the young's modulus $Y = \frac{1}{s_{33}^E}$, the equivalent piezoelectric constant $\overline{d_{33}}$ and $\overline{\varepsilon_{33}^{\sigma}}$.

If the piezoelectric stack is aligned with the z-direction in the ANSYS model, the $\overline{e_{33}}$ can be define using the following commands

$$TB, PIEZ, MATID$$

$$tbdata, 9, \overline{e_{33}}.$$

While the equivalent dielectric constant can be defined also by the PERZ command as

$$MP, PERZ, MATID, \overline{\varepsilon^s_{33}}.$$

A zero voltage boundary condition was applied to one end of the piezoelectric stack while the other end was coupled.So that all nodes should have the same instantaneous voltage. Both piezoelectric stack ends were coupled into two master nodes made to connect the resistor element or a capacitance. CIRCU94 element was used for that purpose. Fig. (14) shows the ANSYS commands used to define the resistance as well as some of the boundary conditions.

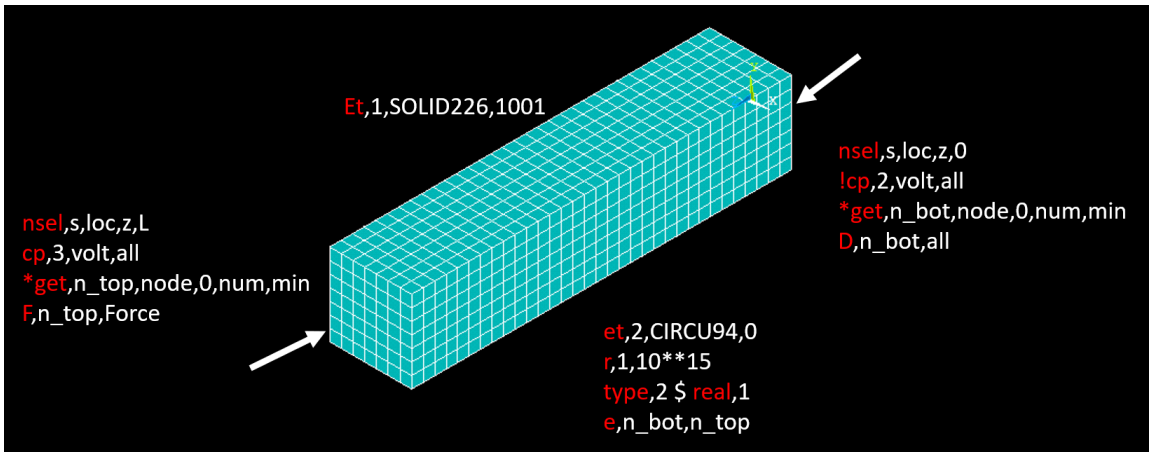

Fig. 14: contour plot for the maximum deformation by ANSYS at force of magnitude of $100N$ and frequency of $10Hz$

The piezoelectric matrix in ANSYS is different from the Piezoelectric Matrix in the IEEE standards as explained below

$$e_{ij}^{IEEE} = \begin{bmatrix} e_{11} & e_{12} & e_{13} \\ e_{21} & e_{22} & e_{23} \\ e_{31} & e_{32} & e_{33} \\ e_{41} & e_{42} & e_{43} \\ e_{51} & e_{52} & e_{53} \\ e_{61} & e_{62} & e_{63} \end{bmatrix} \tag{106}$$

while according to the ANSYS definition it is expressed as follows

$$e_{ij}^{APDL} = \begin{bmatrix} e_{11} & e_{12} & e_{13} \\ e_{21} & e_{22} & e_{23} \\ e_{31} & e_{32} & e_{33} \\ e_{61} & e_{62} & e_{63} \\ e_{41} & e_{42} & e_{43} \\ e_{51} & e_{52} & e_{53} \end{bmatrix}. \tag{107}$$

For the transient analysis, the direct solver (sparse) is used rather than the default iterative solver (PCG). This can be done using the APDL command EQSLV, SPARCE. It's also important to notice that this sparce solver is applicable only in ANSYS full methods only.

The ANSYS PCG solver follows an iterative algorithm which offers a good alternative to more complex sparse direct solvers. These iterative solvers do not require an expensive matrix factorization of the system assembled matrix, and they always run in memory and do only minimal I/O. However, iterative solvers use initial guesses that are random in nature,

but they are chosen to be within an acceptable range of the unknown exact solution. During this iterative process, which is dependent on matrix properties, failure to converge can occur in some cases.

On the other hand, the sparse direct solvers (which include the Block Lanczos method, Gaussian elimination, QR decompositions and the well-known Cholesky method) uses a direct elimination method for the equations, which is different from the iterative solvers. The procedure of the direct elimination factorization method requires the factorization of an initial sparse linear system of equations into a triangular matrix. Then a forward and backward substitution process is done using this triangular matrix system. The disk space required for the aforementioned triangular matrix is always more than the space required for the initial assembly sparse matrix.

CHAPTER 4

ANALYTICAL APPROACH

The analytical method described here was introduced by Feng et al. [70]. This model can be considered complicated; however, it provides good accuracy for the piezoelectric stack modeling. The main advantage of this model over the previous numerical models is that it does not treat the piezoelectric stack as a homogeneous body; it treats each layer as a separate component affected by different stress and strain values; therefore, they generate different voltages.

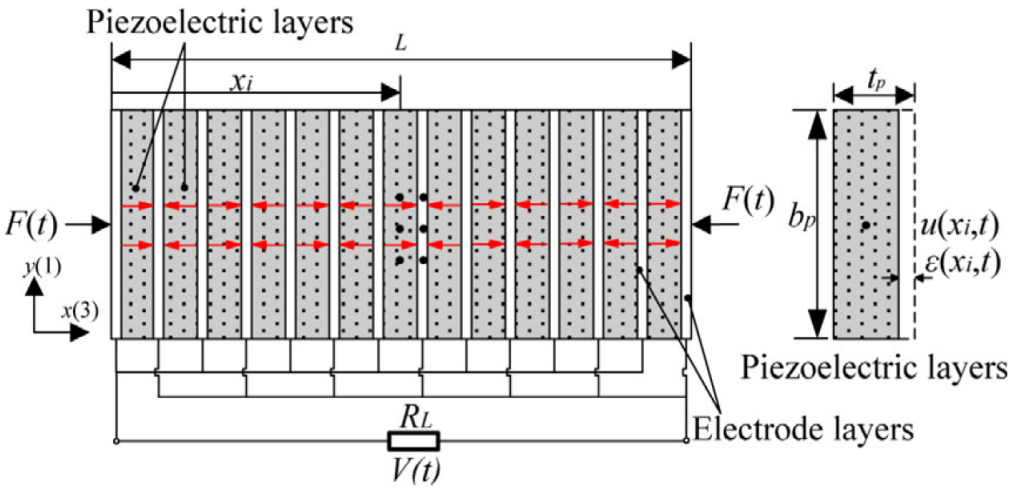

Fig. 15: Piezoelectric multi-layer Stack Schematic [70]

The equations of motion of the piezoelectric stack is derived using the total potential energy method. The kinetic energy can be expressed as

$$T = \frac{1}{2}\int_0^L A\rho(\frac{\partial u}{\partial t})^2 dx \tag{108}$$

$$U = \frac{1}{2}\int_0^L A(\sigma_3 S_3 - E_3 D_3)dx \tag{109}$$

where $u(t)$ is the axial displacement of a certain location on the stack while $\phi(t)$ is the electric potential. The work done by the external force is expressed as

$$W = \int_0^L (Fu - Q\phi)dx. \tag{110}$$

Accordingly, the total energy of the stack can be expressed as

$$\pi = T - U + W. \tag{111}$$

Applying Hamilton's principle to Eq. (110) we get

$$\delta \int_{t_1}^{t_2} \pi dt = \delta \int_{t_1}^{t_2} (T - U + W)dt = 0. \tag{112}$$

Substituting Eqs.(108), (109) and (110) into Eq.(111) we get

$$\int_{t_1}^{t_2} \left\{ \left[\frac{1}{2} \int_0^L A\rho (\frac{\partial u}{\partial t})^2 dx \right] - \left[(\frac{1}{2} \int_0^L A(\sigma_3 S_3 - E_3 D_3)dx) \right] + \left[\int_0^L (Fu - Q\phi)dx \right] \right\} dt = 0. \tag{113}$$

which can be expressed as

$$\delta \int_{t_1}^{t_2} \int_0^L \left\{ \frac{1}{2} A\rho (\frac{\partial u}{\partial t})^2 - \frac{1}{2} A(\sigma_3 S_3 - E_3 D_3) + Fu - Q\phi \right\} dxdt = 0. \tag{114}$$

Performing the variational operation for Eq. (114) we get

$$\begin{aligned} \int_{t_1}^{t_2} \int_0^L \{ & A\rho \frac{\partial u}{\partial t} \frac{\partial \delta u}{\partial t} - Ac_{33}^E \frac{\partial u}{\partial x} \frac{\partial \delta u}{\partial x} \\ & - Ae_{33} \frac{\partial \delta \phi}{\partial x} \frac{\partial u}{\partial x} - \quad Ae_{33} \frac{\partial \phi}{\partial x} \frac{\delta \partial u}{\partial x} + A\varepsilon_{33}^s \frac{\partial \phi}{\partial x} \frac{\partial \delta \phi}{\partial x} \\ & + F\delta u - Q\delta \phi \Big\} dxdt = 0. \end{aligned} \tag{115}$$

Knowing that δu at the time t extreme limits (t_2 and t_1) equals to zero, and by performing

integration by parts for the first term we get

$$\int_{t_1}^{t_2}\int_0^L \left\{ A\rho \frac{\partial u}{\partial t}\frac{\partial \delta u}{\partial t} \right\} dxdt = \int_0^L \left[A\rho \delta u \frac{\partial u}{\partial t}\bigg|_{t_1}^{t_2} \right] dx - \int_{t_1}^{t_2}\int_0^L \left[A\rho\delta u \frac{\partial^2 u}{\partial t^2} dxdt \right] dt \quad (116)$$

$$= -\int_{t_1}^{t_2}\int_0^L \left[A\rho\delta u \frac{\partial^2 u}{\partial t^2} dxdt \right] dt. \quad (117)$$

Using the same method for the rest of the terms in Eq.(115) we get

$$\int_{t_1}^{t_2}\int_0^L \Big\{ \left(-A\rho\frac{\partial^2 u}{\partial t^2} + Ac_{33}^E \frac{\partial^2 u}{\partial x^2} + Ae_{33}\frac{\partial^2 \phi}{\partial x^2} + F \right) \delta u + \left(Ae_{33}\frac{\partial^2 u}{\partial x^2} - A\varepsilon_{33}^s \frac{\partial^2 \phi}{\partial x^2} - Q \right) \delta\phi \Big\} dxdt = 0. \quad (118)$$

Therefore, the two equations of motion can be extracted from Eq.(118):

$$-A\rho\frac{\partial^2 u}{\partial t^2} + Ac_{33}^E \frac{\partial^2 u}{\partial x^2} + Ae_{33}\frac{\partial^2 \phi}{\partial x^2} + F = 0 \quad (119)$$

and

$$Ae_{33}\frac{\partial^2 u}{\partial x^2} - A\varepsilon_{33}^s \frac{\partial^2 \phi}{\partial x^2} - Q = 0. \quad (120)$$

Since we are dealing with energy harvesting application (not actuation), there are no electric changers applied on the surface of the piezoelectric stack, which requires that $Q(x,t) = 0$. Therefore, second equation of motion can be written as

$$e_{33}\frac{\partial^2 u}{\partial x^2} - \varepsilon_{33}^s \frac{\partial^2 \phi}{\partial x^2} = 0. \quad (121)$$

The equation above can be rewritten as

$$\frac{\partial^2 \phi}{\partial x^2} = \frac{e_{33}}{\varepsilon_{33}^s}\frac{\partial^2 u}{\partial x^2}. \quad (122)$$

Substituting Eq.(122) into Eq.(119) we get

$$\boxed{\frac{\partial^2 u}{\partial t^2} + \frac{c}{\rho A}\frac{\partial u}{\partial t} - \frac{k}{\rho}\frac{\partial^2 u}{\partial x^2} = f(x,t)} \tag{123}$$

where

$$k = c_{33}^E + \frac{e_{33}^2}{\varepsilon_{33}^s}$$

$$f(x,t) = \frac{F(x,t)}{\rho A}.$$

The homogeneous solution for Eq. (123) can be expressed in the following form

$$u(x,t) = X(x)T(t) \tag{124}$$

where $X(x)$ is the mode shape function while $T(t)$ is the system response in the time domain, which can be rewritten as

$$u(x,t) = X_n(x)T_n(t) \tag{125}$$

where T_n and X_n can be expressed as

$$T_n = \frac{a_0\left[1-(-1)^n\right]}{\rho AL\omega_n}\left[1 - \frac{\omega_n^2}{\omega_{dn}^2}e^{-\zeta_n\omega_n t}cos(\omega_{dn}t - \theta_{n0})\right] \tag{126}$$

$$+\sum_{m=1}^{\infty}\frac{2\left[1-(-1)^n\right]}{\rho AL\left\{\left[\omega_n^2-(m\omega)^2\right]^2+(2\zeta_n\omega_n m\omega)^2\right\}^{\frac{1}{2}}}\left[a_m\cos(m\omega t-\theta_{nm}) + b_m sin(m\omega t - \theta_{nm})\right] \tag{127}$$

where $w_n = \frac{n\pi}{L}\frac{k}{\rho}$, $\zeta_n = \frac{cL}{2n\pi A\sqrt{\rho k}}$ and $\omega_{dn} = \omega_n\sqrt{1-\zeta_n^2} = \frac{1}{2\rho AL}\sqrt{\rho k(2n\pi A)^2 - c^2L^2}$

$$X_n = b_n cos(\frac{n\pi x}{L}). \tag{128}$$

Noting that the Fourier series was used to express the force as follows

$$F(t) = \frac{a_0}{2} + \sum_{m=1}^{N_f}\left[a_m\cos(m\omega t) + b_m\sin(m\omega t)\right] \tag{129}$$

where N_f is the number of harmonic terms and a_0, a_m and b_m are the Fourier coefficients. Therefore, $u(x,t)$ can be written as

$$\begin{aligned} u(x,t) &= \sum_{n=1}^{\infty} X_n(x)T_n(t) \\ &= \sum_{m=1}^{\infty} cos(\frac{n\pi x}{L})\frac{a_0\left[1-(-1)^n\right]}{\rho AL\omega_n}\left[1 - \frac{\omega_n^2}{\omega_{dn}^2}e^{-\zeta_n\omega_n t}cos(\omega_{dn}t - \theta_{n0})\right] \\ &+ \sum_{m=1}^{N_f}\frac{2\left[1-(-1)^n\right]}{\rho AL\left\{\left[\omega_n^2 - (m\omega)^2\right]^2 + (2\zeta_n\omega_n m\omega)^2\right\}^{\frac{1}{2}}} \qquad (130) \\ &\left(a_m\cos\left(m\omega t - \theta_{nm}\right) + b_m sin(m\omega t - \theta_{nm})\right) \qquad (131) \end{aligned}$$

where N_f is the number of harmonic terms. We have the strain $S_3(x,t)$ expressed as

$$S_3(x,t) = \frac{\partial u(x,t)}{\partial x} = \frac{\partial X(x)}{\partial x}T(t) \tag{132}$$

by substituting Eq.(130) into Eq.(132) we get

$$S_3(x,t) = \sum_{n=1}^{\infty}(-\frac{n\pi}{L})sin(\frac{n\pi x}{L})T_n(t). \tag{133}$$

Also, the voltage can be analytically obtained from Eq.(134):

$$\varphi(t) = \frac{Ae_{33}}{C_p} e^{\frac{-t}{R_L C_p}} \sum_{i=1}^{p} \int e^{\frac{t}{R_L C_p}} \frac{dS_3(x_i)}{dt} dt. \tag{134}$$

Substituting with the value of $\frac{dS_3(x_i)}{dt}$ we get

$$\varphi(t) = \frac{Ae_{33}}{C_p} e^{\frac{-t}{R_L C_p}} \sum_{i=1}^{p} \int e^{\frac{t}{R_L C_p}} \sum_{n=1}^{\infty} \left(-\frac{n\pi}{L}\right) sin\left(\frac{n\pi x}{L}\right) \dot{T}_n dt. \tag{135}$$

The equation above can be reorganized and expressed in the form:

$$\varphi(t) = \frac{Ae_{33}}{C_p} e^{\frac{-t}{R_L C_p}} \sum_{i=1}^{p} \sum_{n=1}^{\infty} \left(-\frac{n\pi}{L}\right) sin\left(\frac{n\pi x}{L}\right) \int e^{\frac{t}{R_L C_p}} \dot{T}_n dt. \tag{136}$$

We can get the value of $\dot{T}_n$ from Eq.(126).

$$\begin{aligned} \dot{T}_n = \frac{a_0\left[1-(-1)^n\right]}{\rho AL\omega_n} & \left[-\frac{\omega_n^2}{\omega_{dn}^2}\left(-\zeta_n\omega_n e^{-\zeta_n\omega_n t}\cos\left(\omega_{dn}t-\theta_{n0}\right)+e^{-\zeta_n\omega_n t}\omega_{dn}\sin\left(\omega_{dn}t-\theta_{n0}\right)\right)\right] \\ & + \sum_{m=1}^{\infty} \frac{2\left[1-(-1)^n\right]m\omega}{\rho AL\left\{\left[\omega_n^2-(m\omega)^2\right]^2+\left(2\zeta_n\omega_n m\omega\right)^2\right\}^{\frac{1}{2}}} \\ & \times\left[-a_m\sin\left(m\omega t-\theta_{nm}\right)+b_m\ cos(m\omega t-\theta_{nm})\right] \end{aligned} \tag{137}$$

In order to make the equation smaller assume the following:

$$T_a = \frac{2\left[1-(-1)^n\right]m\omega}{\rho AL\left\{\left[\omega_n^2-(m\omega)^2\right]^2+\left(2\zeta_n\omega_n m\omega\right)^2\right\}^{\frac{1}{2}}} \tag{138}$$

$$S_n = \left(-\frac{n\pi}{L}\right) sin\left(\frac{n\pi x}{L}\right) \tag{139}$$

Therefore, the generated voltage can be expressed as:

$$\therefore \varphi(t) = \frac{Ae_{33}}{C_p} e^{\frac{-t}{R_L C_p}} \sum_{i=1}^{p} \sum_{n=1}^{\infty} S_n \int e^{\frac{t}{R_L C_p}} \Big\{ - \frac{\omega_n^2}{\omega_{dn}^2} (-\zeta_n \omega_n e^{-\zeta_n \omega_n t} \cos(\omega_{dn} t - \theta_{n0}) + e^{-\zeta_n \omega_n t} \omega_{dn} \sin(\omega_{dn} t - \theta_{n0})) + \sum_{m=1}^{\infty} T_a \left[-a_m \sin(m\omega t - \theta_{nm}) + b_m \cos(m\omega t - \theta_{nm}) \right] \Big\} dt \tag{140}$$

$$\therefore \varphi(t) = \frac{Ae_{33}}{C_p} e^{\frac{-t}{R_L C_p}} \sum_{i=1}^{p} \sum_{n=1}^{\infty} S_n \int e^{\frac{t}{R_L C_p}} \Big\{ - \frac{\omega_n^2}{\omega_{dn}^2} \big\{ -\zeta_n \omega_n e^{-\zeta_n \omega_n t} \cos(\omega_{dn} t - \theta_{n0}) + e^{-\zeta_n \omega_n t} \omega_{dn} \sin(\omega_{dn} t - \theta_{n0}) \big\} + \sum_{m=1}^{\infty} T_a \left[-a_m \sin(m\omega t - \theta_{nm}) + b_m \sin(m\omega t - \theta_{nm}) \right] \Big\} dt \tag{141}$$

$$\therefore \varphi(t) = \frac{Ae_{33}}{C_p} e^{\frac{-t}{R_L C_p}} \sum_{i=1}^{p} \sum_{n=1}^{\infty} S_n \int \left(\varphi_3 + \sum_{m=1}^{\infty} T_{nm} \left[\varphi_1 + \varphi_2 \right] \right) dt. \tag{142}$$

Now we divide the integration into three parts to make it simpler:

$$\varphi_1 = \int e^{\frac{t}{R_L C_p}} \left([-a_m \sin(m\omega t - \theta_{nm})] \right) dt \tag{143}$$

$$\varphi_2 = \int e^{\frac{t}{R_L C_p}} \left([b_m \cos(m\omega t - \theta_{nm})] \right) dt \tag{144}$$

$$\varphi_3 = \int e^{\frac{t}{R_L C_p}} \frac{a_0 \left[1 - (-1)^n \right]}{\rho A L \omega_n} \Big\{ - \frac{\omega_n^2}{\omega_{dn}^2} (-\zeta_n \omega_n e^{-\zeta_n \omega_n t} \cos(\omega_{dn} t - \theta_{n0}) + e^{-\zeta_n \omega_n t} \omega_{dn} \sin(\omega_{dn} t - \theta_{n0})) \Big\} dt. \tag{145}$$

Now performing integration for φ_1

$$\varphi_1 = \int e^{\frac{t}{R_L C_p}} \left([-a_m \sin\left(m\omega t - \theta_{nm}\right)]\right) dt. \tag{146}$$

Integration by parts:

$$\varphi_1 = -R_L C_p e^{\frac{t}{R_L C_p}} a_m \sin\left(m\omega t - \theta_{nm}\right) + \int R_L C_p e^{\frac{t}{R_L C_p}} a_m m\omega \cos\left(m\omega t - \theta_{nm}\right) dt + C_1 \tag{147}$$

where C_1 is an integration constant.

$$\varphi_1 = -R_L C_p a_m \left(e^{\frac{t}{R_L C_p}} \sin\left(m\omega t - \theta_{nm}\right) - \int e^{\frac{t}{R_L C_p}} m\omega \cos\left(m\omega t - \theta_{nm}\right) dt \right) + C_1 \tag{148}$$

$$\begin{aligned} \varphi_1 = -R_L C_p a_m \big\{ & e^{\frac{t}{R_L C_p}} \sin\left(m\omega t - \theta_{nm}\right) - \big\{ R_L C_p m\omega e^{\frac{t}{R_L C_p}} \cos\left(m\omega t - \theta_{nm}\right) \\ & + \int R_L C_p (m\omega)^2 e^{\frac{t}{R_L C_p}} \sin\left(m\omega t - \theta_{nm}\right) dt + C_2 \big\} \big\} + C_1. \end{aligned} \tag{149}$$

where C is an new integration constant which combines C_1 with the new integration constant.

$$\begin{aligned} \varphi_1 = R_L C_p a_m \big\{ & -e^{\frac{t}{R_L C_p}} \sin\left(m\omega t - \theta_{nm}\right) + R_L C_p m\omega \; e^{\frac{t}{R_L C_p}} \cos\left(m\omega t - \theta_{nm}\right) \big\} \\ & + \int a_m (R_L C_p m\omega)^2 \; e^{\frac{t}{R_L C_p}} \sin\left(m\omega t - \theta_{nm}\right) dt + C \end{aligned} \tag{150}$$

$$\therefore \int e^{\frac{t}{R_L C_p}} \left([-a_m \sin(m\omega t - \theta_{nm})]\right) dt - \int a_m (R_L C_p m\omega)^2 \, e^{\frac{t}{R_L C_p}} \sin(m\omega t - \theta_{nm}) dt$$
$$= R_L C_p a_m \left(-e^{\frac{t}{R_L C_p}} \sin(m\omega t - \theta_{nm}) + R_L C_p m\omega \, e^{\frac{t}{R_L C_p}} \cos(m\omega t - \theta_{nm}) \right) + C \quad (151)$$

$$-(1 + (R_L C_p m\omega)^2) \int e^{\frac{t}{R_L C_p}} \left([a_m \sin(m\omega t - \theta_{nm})]\right) dt$$
$$= R_L C_p a_m \left(-e^{\frac{t}{R_L C_p}} \sin(m\omega t - \theta_{nm}) + R_L C_p m\omega \, e^{\frac{t}{R_L C_p}} \cos(m\omega t - \theta_{nm}) \right) + C \quad (152)$$

$$\varphi_1 = \int e^{\frac{t}{R_L C_p}} \left([a_m \cos(m\omega t - \theta_{nm})]\right) dt \quad (153)$$
$$= \frac{R_L C_p a_m e^{\frac{t}{R_L C_p}} \left(\sin(m\omega t - \theta_{nm}) - R_L C_p m\omega \, \cos(m\omega t - \theta_{nm})\right)}{(1 + (R_L C_p m\omega)^2)} + C \quad (154)$$

We have the equation for φ expressed as

$$\varphi_2 = \int e^{\frac{t}{R_L C_p}} \left([b_m \cos(m\omega t - \theta_{nm})]\right) dt. \quad (155)$$

Now performing integration for to Eq.(155) we get

$$\varphi_2 = b_m R_L C_p e^{\frac{t}{R_L C_p}} \cos(m\omega t - \theta_{nm}) + \int b_m R_L C_p m\omega e^{\frac{t}{R_L C_p}} \sin(m\omega t - \theta_{nm}) dt + C_3 \quad (156)$$

where C_3 is an integration constant.

Eq.(156) can be rewritten as

$$\varphi_2 = b_m R_L C_p \left\{ e^{\frac{t}{R_L C_p}} \cos\left(m\omega t - \theta_{nm}\right) + \int m\omega \; e^{\frac{t}{R_L C_p}} \sin\left(m\omega t - \theta_{nm}\right) dt \right\} + C_3 \quad (157)$$

$$\begin{aligned} \varphi_2 = b_m R_L C_p \big\{ & e^{\frac{t}{R_L C_p}} \cos\left(m\omega t - \theta_{nm}\right) + \left[m\omega R_L C_p e^{\frac{t}{R_L C_p}} \sin\left(m\omega t - \theta_{nm}\right) \right. \\ & \left. - \int \left(m\omega\right)^2 R_L C_p e^{\frac{t}{R_L C_p}} \cos\left(m\omega t - \theta_{nm}\right) dt \right] \big\} + C_3 \end{aligned} \quad (158)$$

$$\begin{aligned} \therefore \int e^{\frac{t}{R_L C_p}} \left(\left[b_m \cos\left(m\omega t - \theta_{nm}\right) \right] \right) dt = \; & b_m R_L C_p \big\{ e^{\frac{t}{R_L C_p}} \cos\left(m\omega t - \theta_{nm}\right) \\ + \left[m\omega R_L C_p e^{\frac{t}{R_L C_p}} \sin\left(m\omega t - \theta_{nm}\right) - \int \left(m\omega\right)^2 R_L C_p e^{\frac{t}{R_L C_p}} \cos\left(m\omega t - \theta_{nm}\right) dt \right] & \big\} + C_3 \end{aligned} \quad (159)$$

$$\begin{aligned} & \therefore \left(1 + \left(R_L C_p m\omega\right)^2\right) \int e^{\frac{t}{R_L C_p}} \left(b_m \sin\left(m\omega t - \theta_{nm}\right) \right) dt \\ & = \; b_m R_L C_p \left\{ e^{\frac{t}{R_L C_p}} \cos\left(m\omega t - \theta_{nm}\right) + m\omega R_L C_p e^{\frac{t}{R_L C_p}} \sin\left(m\omega t - \theta_{nm}\right) \right\} + C_3 \end{aligned} \quad (160)$$

$$\begin{aligned} \therefore \varphi_2 &= \int e^{\frac{t}{R_L C_p}} \left(b_m \sin\left(m\omega t - \theta_{nm}\right) \right) dt \\ &= \frac{b_m R_L C_p e^{\frac{t}{R_L C_p}} \left\{ \cos\left(m\omega t - \theta_{nm}\right) + m\omega R_L C_p \sin\left(m\omega t - \theta_{nm}\right) \right\}}{1 + \left(R_L C_p m\omega\right)^2} + C_3. \end{aligned} \quad (161)$$

Now integrating φ_3

$$\varphi_3 = \int e^{\frac{t}{R_L C_p}} \frac{a_0\left[1-(-1)^n\right]}{\rho A L \omega_n}\Big\{ -\frac{\omega_n^2}{\omega_{dn}^2}(-\zeta_n\omega_n e^{-\zeta_n\omega_n t}\cos\left(\omega_{dn}t-\theta_{n0}\right) + e^{-\zeta_n\omega_n t}\omega_{dn}\sin\left(\omega_{dn}t-\theta_{n0}\right))\Big\}dt.$$

by following the same integration and substitution procedure as for φ_1 and φ_2 we get

$$\varphi_3 = \frac{a_0\left[1-(-1)^n\right]}{\rho A L \omega_n}\Big\{R_L C_p e^{\frac{t}{R_L C_p}} - \frac{\omega_n^2}{\omega_{dn}^2(\frac{1}{R_L C_p}-\zeta_n\omega_n)} \frac{\frac{1}{(\frac{1}{R_L C_p}-\zeta_n\omega_n)}e^{t(\frac{1}{R_L C_p}-\zeta_n\omega_n)}\cos\left(\omega_{dn}t-\theta_{n0}\right) + \left\{\frac{\omega_{dn}}{(\frac{1}{R_L C_p}-\zeta_n\omega_n)^2}e^{t(\frac{1}{R_L C_p}-\zeta_n\omega_n)}\right\}}{1+\left(\frac{\omega_{dn}}{(\frac{1}{R_L C_p}-\zeta_n\omega_n)}\right)^2}\Big\} + C. \quad (162)$$

Combining all the resulting equations, we will finally get the generated voltage equation

$$\begin{aligned}\varphi(t) = {} & \frac{Ae_{33}}{C_p}e^{\frac{-t}{R_L C_p}}\Big\{\sum_{i=1}^{p}\sum_{n=1}^{\infty}\left(-\frac{n\pi}{L}\right)sin\left(\frac{n\pi x}{L}\right)\Big\{\frac{a_0\left[1-(-1)^n\right]}{\rho A L\omega_n} \\ & \times\Big\{R_L C_p e^{\frac{t}{R_L C_p}} - \frac{\omega_n^2}{\omega_{dn}^2(\frac{1}{R_L C_p}-\zeta_n\omega_n)} \\ & \times \frac{\frac{1}{(\frac{1}{R_L C_p}-\zeta_n\omega_n)}e^{t(\frac{1}{R_L C_p}-\zeta_n\omega_n)}\cos\left(\omega_{dn}t-\theta_{n0}\right) + \left\{\frac{\omega_{dn}}{(\frac{1}{R_L C_p}-\zeta_n\omega_n)^2}e^{t(\frac{1}{R_L C_p}-\zeta_n\omega_n)}\right\}}{1+\left(\frac{\omega_{dn}}{(\frac{1}{R_L C_p}-\zeta_n\omega_n)}\right)^2}\Big\} \\ & + \sum_{m=1}^{\infty}\frac{2[1-(-1)^n]m\omega}{\rho A L\left\{\left[\omega_n^2-(m\omega)^2\right]^2+(2\zeta_n\omega_n m\omega)^2\right\}^{\frac{1}{2}}} \\ & \times\Big\{\frac{R_L C_p a_m e^{\frac{t}{R_L C_p}}\left(\cos\left(m\omega t-\theta_{nm}\right)+R_L C_p m\omega\ \sin\left(m\omega t-\theta_{nm}\right)\right)}{\left(1+\left(R_L C_p m\omega\right)^2\right)} \\ & + \frac{b_m R_L C_p e^{\frac{t}{R_L C_p}}\left\{\sin\left(m\omega t-\theta_{nm}\right)-m\omega R_L C_p\cos\left(m\omega t-\theta_{nm}\right)\right\}}{1+\left(R_L C_p m\omega\right)^2}\Big\}\Big\}\Big\} + C. \end{aligned} \quad (163)$$

At the initial time $t = 0$ *sec*, the piezoelectric stack is under no stress (or strain); therefore, the generated voltage equals zero $\varphi(0) = 0$ which makes the integration constant equal zero, $C = 0$.

MATLAB was used to solve Eq.(163). It was found that for the summation signs, using values of $n = 2$ and $m = 1$ would be sufficient to produce the required results with almost no change in the voltage result. Also, from Eq. (134) it can be seen that the generated voltage $\varphi(t)$ is mainly dependent on the rate of strain taking place inside the material. The rate of strain is mainly dependent on the the n^{th} forced modal response of the piezoelectric stack, which are the first two modal resonances ($n = 2$). Since the force input to the model is a pure sinusoidal wave, the Fourier coefficient a_m is the dominant term in (Eq. 163) and the effect of a_0 and b_m.

For the open circuit condition ($R_L \to \infty$) the voltage equation can be expressed as

$$\varphi(t) = \frac{Ae_{33}}{C_p} \sum S_3(x_i, t). \tag{164}$$

Therefore, for a sinusoidal input, Eq. (163) can be reduced as follows

$$\varphi(t) = \frac{Ae_{33}}{C_p} \sum_{n=1}^{2} \frac{2\left[1 - (-1)^n\right]}{\rho AL \left\{\left[\omega_n^2 - \omega^2\right]^2 + \left(2\zeta_n \omega_n \omega\right)^2\right\}^{\frac{1}{2}}} \left[a_1 \cos\left(\omega t\right)\right]. \tag{165}$$

Noting that the dominant terms in Eq. (163) are the Fourier coefficients a_0, a_m and b_m Also, the electric current can be calculated using the following equation

$$i(t) = C_p \frac{d\varphi(t)}{dt} = Ae_{33} \sum_{i=1}^{p} S_3(x_i, t). \tag{166}$$

The instant power accordingly can be calculated by substituting the values of the voltage

from Eq.(163) in Eq.(167).

$$P_R(t) = \frac{\varphi(t)}{R_L} \tag{167}$$

where R_L is the resistive load value. Noting that in the current work, only the open circuit case was tested. For an open circuit case the resistance is assumed to be equal 10^{15}.

CHAPTER 5

EXPERIMENT SETUP

The purpose of the experimental setup is to locate the resonance frequency of the FPEH as well as specifying the voltage generated at this frequency. Accordingly, a shaker system was required. This shaker system is capable of generating a sweep function in the range of the natural frequency of the harvester as well as a vibration magnitude that is compatible with the harvester that is being tested. The result of the FEA (ANSYS modal and harmonic models) were verified using the experimental readings.

Another important use for the experimental results is to choose a suitable value for the damping coefficient for the harvester in the ANSYS. One of the challenges in ANSYS simulations is that the deformation tends to infinity at the resonance frequency. That requires defining a suitable damping coefficient for the harvester components or for the assembly as a whole. There are no analytical or numerical methods found in the literature that can predict these damping coefficients. The only way to do it is to define it using the experimental values by tuning the coefficients so that the system response in the ANSYS model matches the experimental response.

The setup of the experiment is shown in Fig. (16). The PM 100 Electrodynamic Vibration Exciterwas (shaker) used; this shaker is capable of producing a force output of $100lbs$ peak and a maximum displacement of $0.5inch$ amplitude (peak-peak). The maximum acceleration and frequency this shaker can produce are $100g's$ and $7000Hz$, respectively for an unloaded shaker.

Fig. 16: Dynamic experiment setup of Flextensional Piezoelectric Energy Harvester

On the shaker's top the harvester was attached using an $M3$ screw, and a piezoelectric accelerometer was attached to it as well Fig. (17)

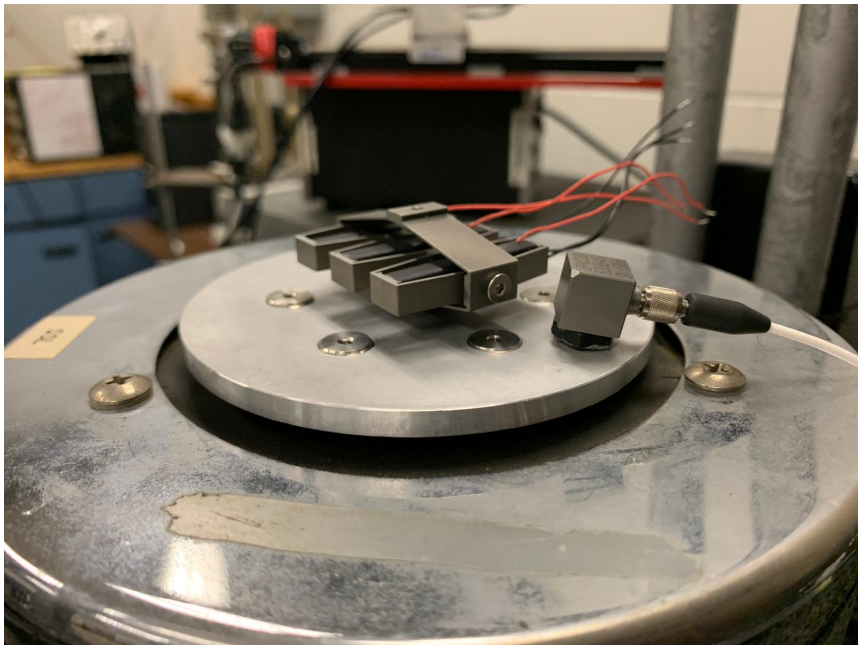

Fig. 17: Multistage Piezoelectric Energy Harvester and an Accelerometer mounted on the shaker's top plate.

5.1 VIBRATION EXCITER MAXIMUM RESPONSE

The maximum allowable shaker acceleration depends on the weight of the load attached to it, the mass of the fixture base attached on it (where the harvester is mounted), the mass of the harvester itself, the weight of the screws and the sensing devices as shown in Eq. (168)

$$A_{max} = \frac{F_R}{W_{ME} + W_{TA} + W_F} \tag{168}$$

where

A_{max} = Maximum allowable table acceleration in g's peak

F_R = Rated force of the shaker"$100lb$"

W_{ME} = Weight of the moving element

W_{TA} = Weight of the test article

W_F = Weight of the bolts, screws, and sensors.

5.2 VIBRATION EXCITER CONTROL

To operate the shaker, a power amplifier is required. The power amplifier model SL500VCF was used. This power amplifier can provide power output of $450Watt_{rms}$. It can match the performance of the PM 100 shaker when connected for low impedance.

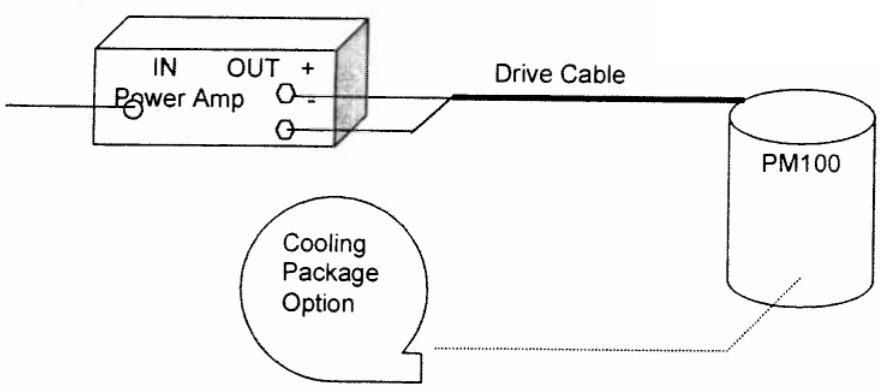

Fig. 18: Simplified Diagram Connection for the Shaker with the Power Amplifier "the Cooler Option Was Not Used in the Experiment"

There are two ways to control the shaker to perform a sweep motion, either to connect it to a sweep generator (Fig. 19) or to connect it to LABVIEW.

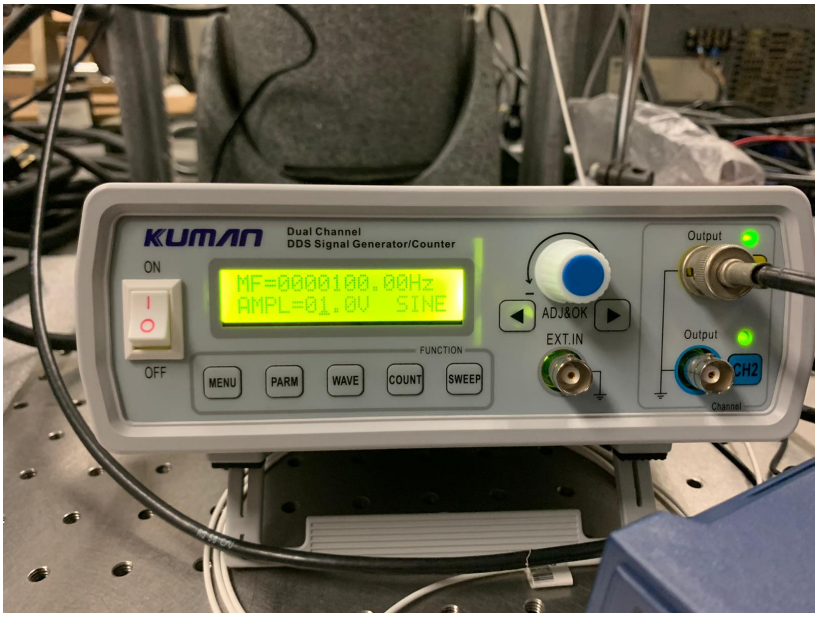

Fig. 19: Dual Channel Function Generator

As mentioned earlier, the accelerometer was attached to the shaker base using wax. Then the extension cable of the accelerometer was connected using a BNC connector to a PCB 482C Series 4-Channel Signal Conditioner shown in Fig. (20)

Fig. 20: PCB 482C Series 4-Channel Signal Conditioner

The frequency range applied to the shaker was 20 to 300Hz. The problem with using

this setup is that when we attempt to apply a sweep function, the shaker output acceleration increases as the frequency increases. Designing a control algorithm to use the acceleration reading as a feedback and then adjusting the output of the shaker such that it maintains fixed acceleration is rather cumbersome. As a result, the experimental results for the voltage output will be presented in the results chapter as $Volts/g's$.

CHAPTER 6

RESULTS

The results chapter is divided into two sections; the first section discusses off-resonance mode while the second section will discuss the resonance mode simulation.

6.1 OFF-RESONANCE MODE RESULTS

The force applied on the flextensional piezoelectric harvester's force amplification frame was adjusted so that the force exerted on piezoelectric multilayer stack becomes $100N$. Noting that, the amplification factor for the FAF is 4.6. Fig. (21) shows a plot of the applied force on the stack.

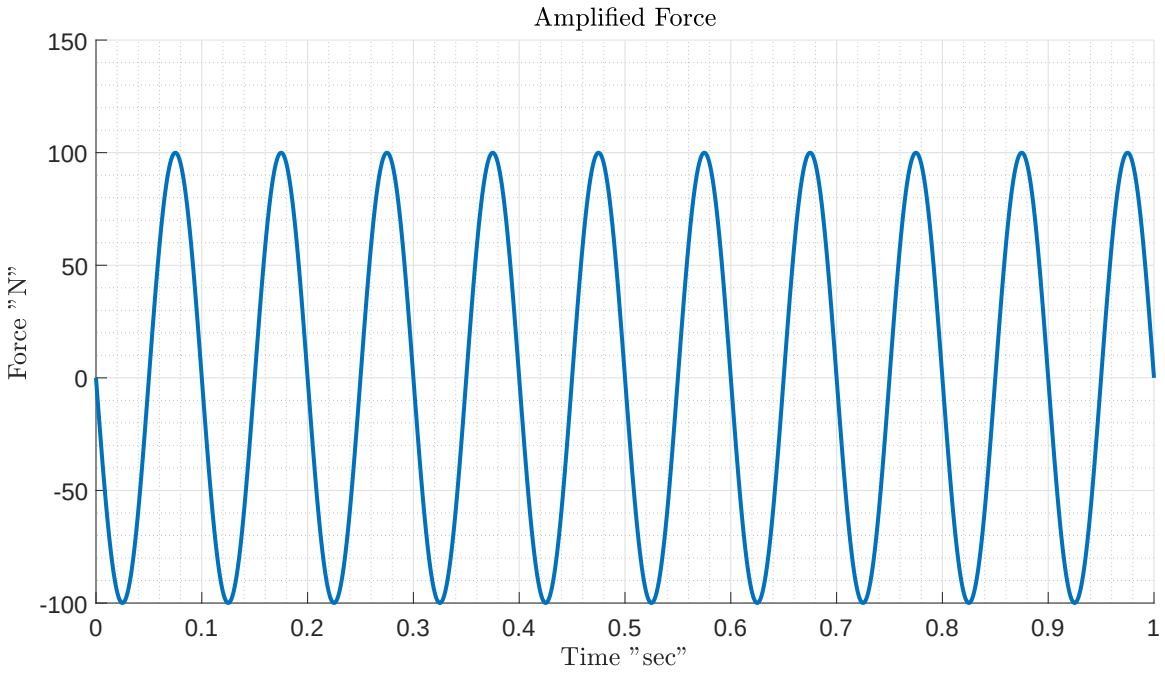

Fig. 21: Amplified force with an amplitude of $100N$ and frequency $10Hz$

The monolithic piezoelectric stack actuator (CeramTech SP505) was used in this study as a harvester instead. The stack is built using 300 piezoelectric layers of 0.1 mm thickness

sandwiched between 301 silver electrodes. The total volume of the stack is $7mm \times 7mm \times 32.40mm$, and its density is $\rho = 7700kg/m^3$.

The main parameters used to model the piezoelectric material are the $s_{33}^E = 24 \times 10^{-12}m^2/N$, $d_{33} = 475pC/N$ and $\varepsilon_{33}^T = 1880$.

The comparison between the models will be based on the root mean square values (RMS) of the voltages output. Since the applied force is sinusoidal in nature and the resulted voltage will follow a sinusoidal behavior too, we can use Eq. (169).

$$V_{rms} = \frac{V_{peak}}{\sqrt{2}} \tag{169}$$

6.1.1 QUASI-STATIC MODEL

The voltage output of the static model can be seen in Fig. (22). The maximum voltage "$V_{max} = V_{peak}$" equals $5.824V$ which yields a root mean square value of $V_{rms} = 4.1182V$.

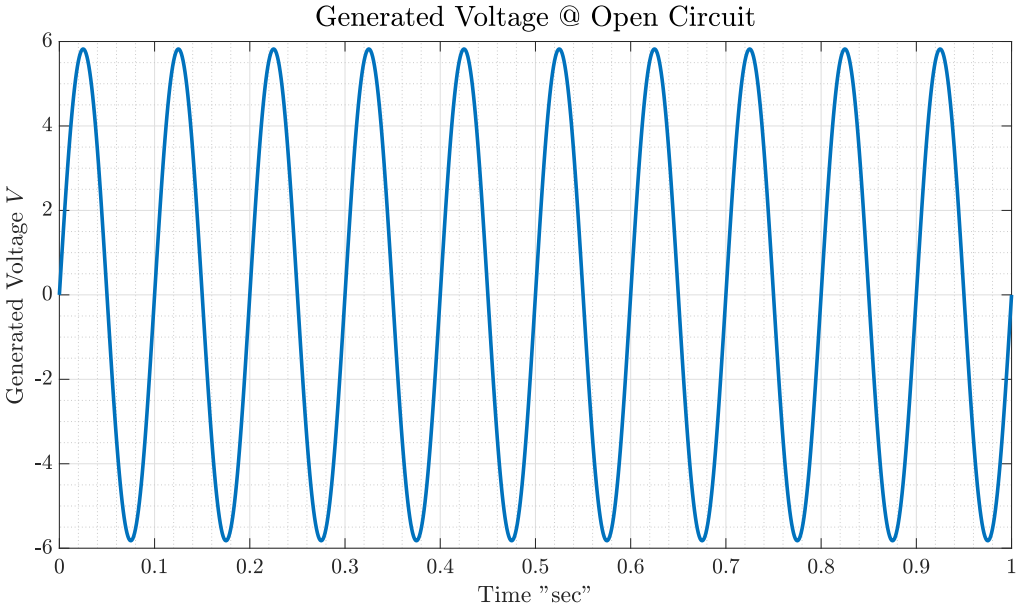

Fig. 22: Static Model Voltage Output

6.1.2 SINGLE DEGREE OF FREEDOM MODEL

The voltage output of the static model can be seen in Fig. (23). The maximum voltage "V_{max}" equals $3.791V$ which yields a root mean square value of $V_{rms} = 2.6806V$.

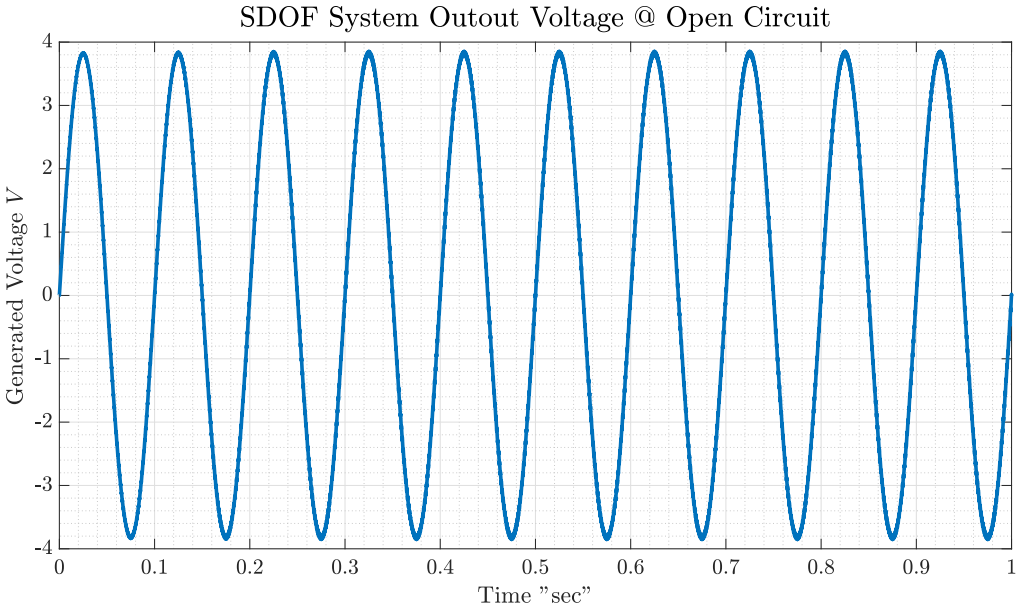

Fig. 23: Single Degree of Freedom Model Output Voltage

6.1.3 ANSYS TRANSIENT MODEL

The mesh Dependence Study was performed on the piezoelectric stack as well as the FPEH in the open circuit condition. In this abstract we present the mesh dependence study carried on the stack under a randomly chosen sinusoidal force of $100N$ and frequency of $11Hz$. Both piezoelectric elements SOLID226 and SOLID227 were tested. As shown, Fig. (24) meshes with an element number ranging from 500 elements to 14850 elements were used and they all gave the same exact result. These 500 elements, minimum threshold was used in the FPEH simulation as well (transient, modal and harmonic analyses).

Contour plots for the generated voltage, maximum deformation and von-mises stress when a force of magnitude 100 and frequency of $10Hz$ are shown in Figs. (25), (26) and (27).

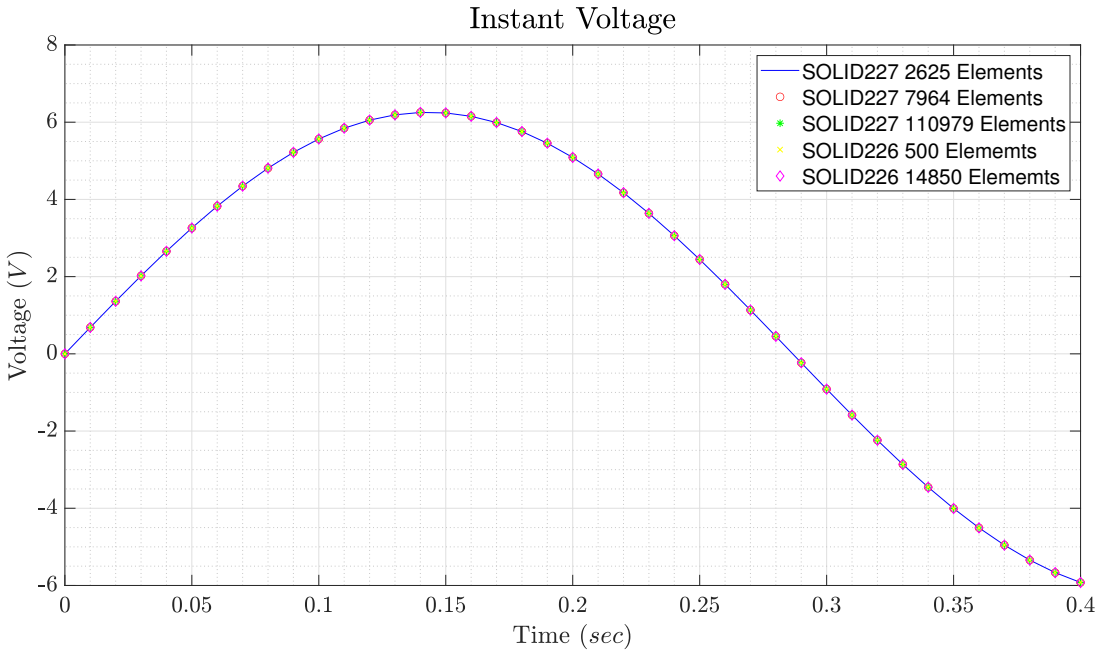

Fig. 24: Piezoelectric Stack Mesh Dependence Study

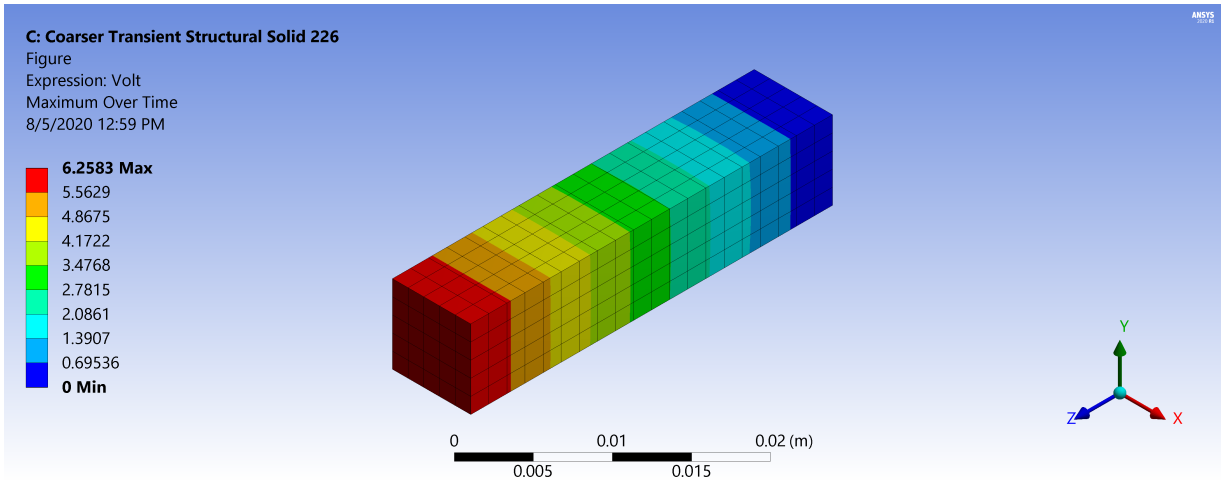

Fig. 25: Contour plot for the maximum generated voltage by ANSYS at force of magnitude of $100N$ and frequency of $10Hz$

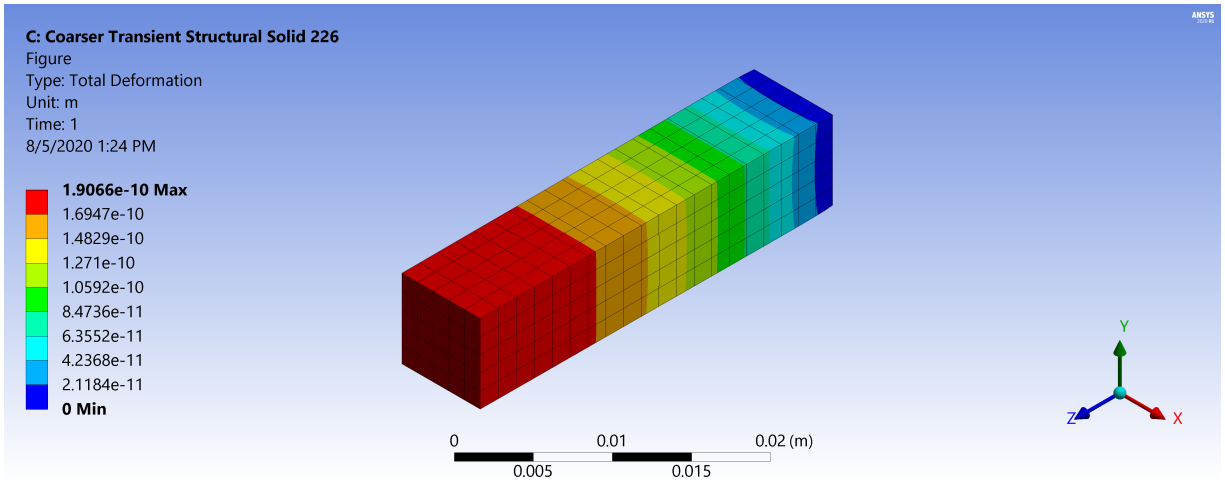

Fig. 26: Contour plot for the maximum deformation by ANSYS at force of magnitude of $100N$ and frequency of $10Hz$

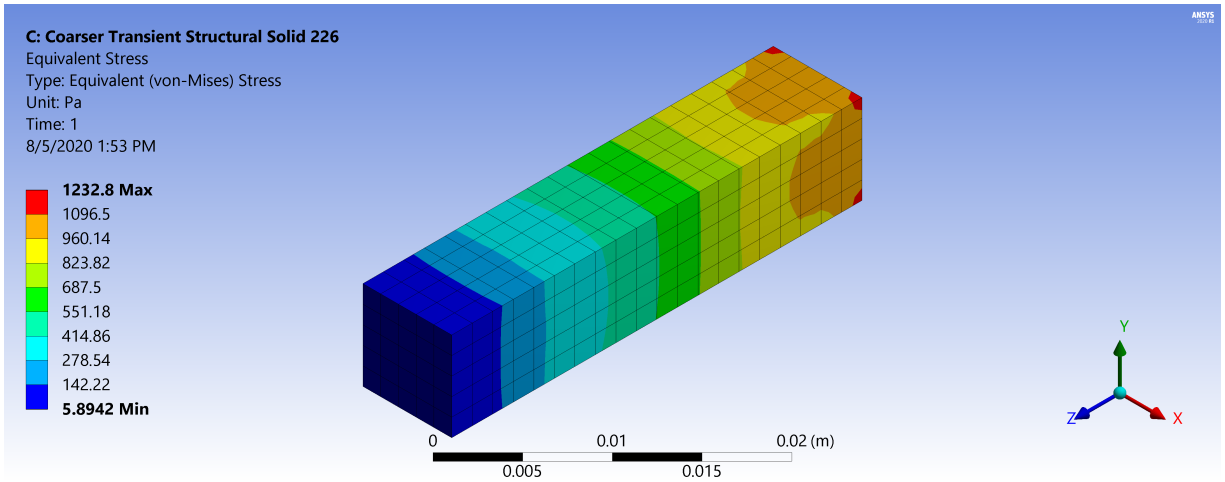

Fig. 27: Contour plot for the maximum stress by ANSYS at force of magnitude of $100N$ and frequency of $10Hz$

The voltage output of the finite element model is presented in Fig. (28). The maximum voltage "V_{max}" equals $6.243V$ which yields a root mean square value of $V_{rms} = 4.4145V$.

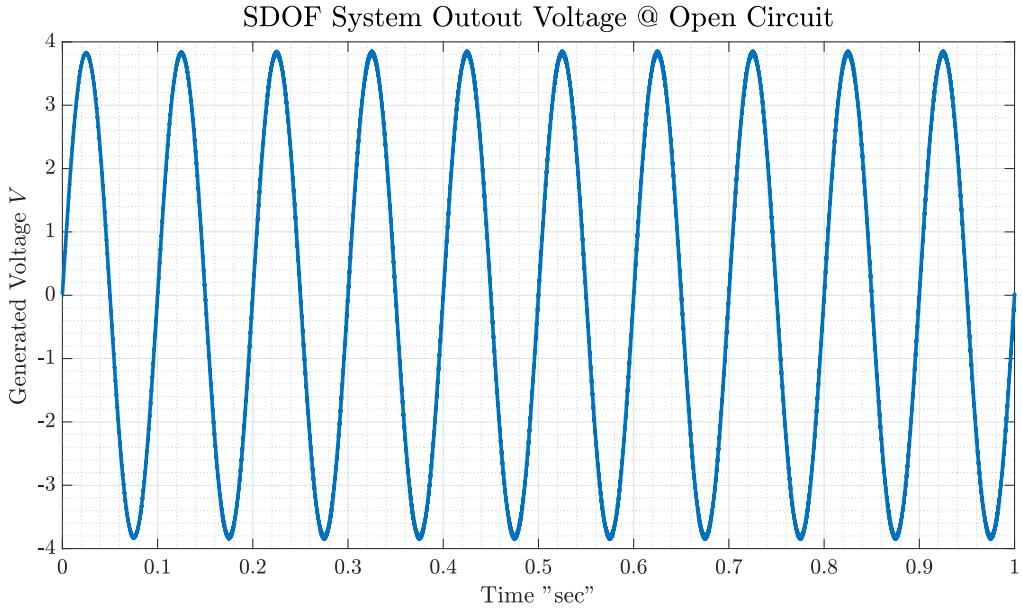

Fig. 28: Single Degree of Freedom Model Output Voltage

6.1.4 THE DISTRIBUTED PARAMETER MODEL "ANALYTICAL MODEL"

The voltage output of the distributed parameter model can be seen in Fig. (29). The maximum voltage "V_{max}" equals $5.406V$ which yields a root mean square value of $V_{rms} = 3.8226V$.

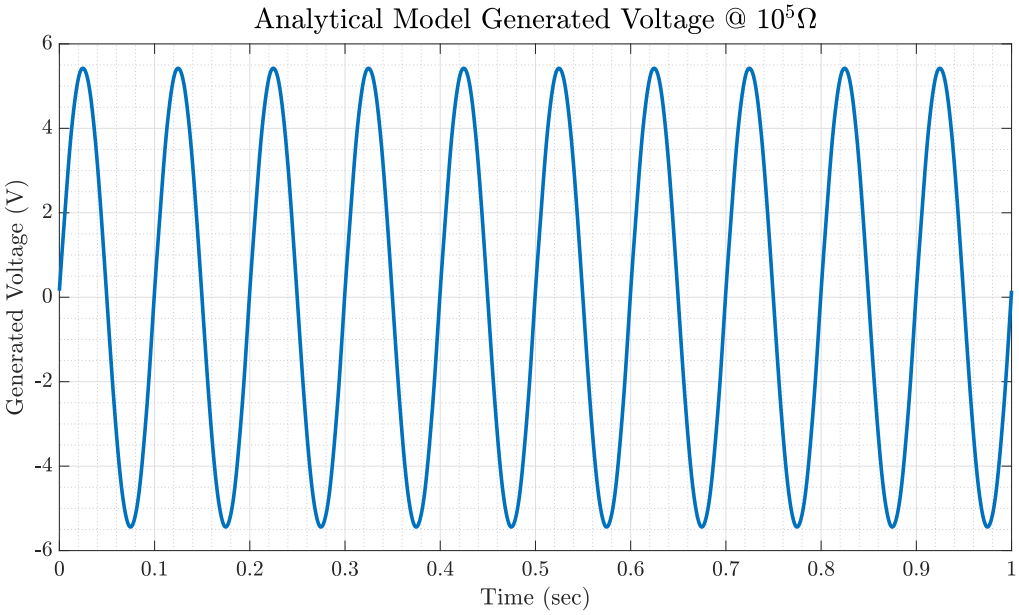

Fig. 29: Analytical Model Generated Voltage

6.1.5 TRANSIENT MODELS DISCUSSION

Fig. (30) shows the generated voltage for the quasi static, SDOF, ANSYS and the distributed parameter models. It can be seen that the experimental results coincides on the expected voltage of the analytical model (the distributed parameter model). Noting that the experimental data used was extracted from the same paper which presented this distributed parameter model [70].

The SDOF model gave the maximum deviation compared to the experimental data. This is because the SDOF model treats the multilayer stack as one bulk object. Also, the SDOF model ignores the damping inside the piezoelectric stack caused by the presence of the electrodes, and it also ignored the strains distribution or the difference in strains between the piezoelectric layers. The RMS error percentage $Erms$ for this case reached 25.1661%.

The ANSYS model can be enhanced if the effect of the capacitance of the piezoelectric stack is taken into account. Fig. (31a) shows equivalent circuits for PZT stacks proposed by Xu et al. [69].

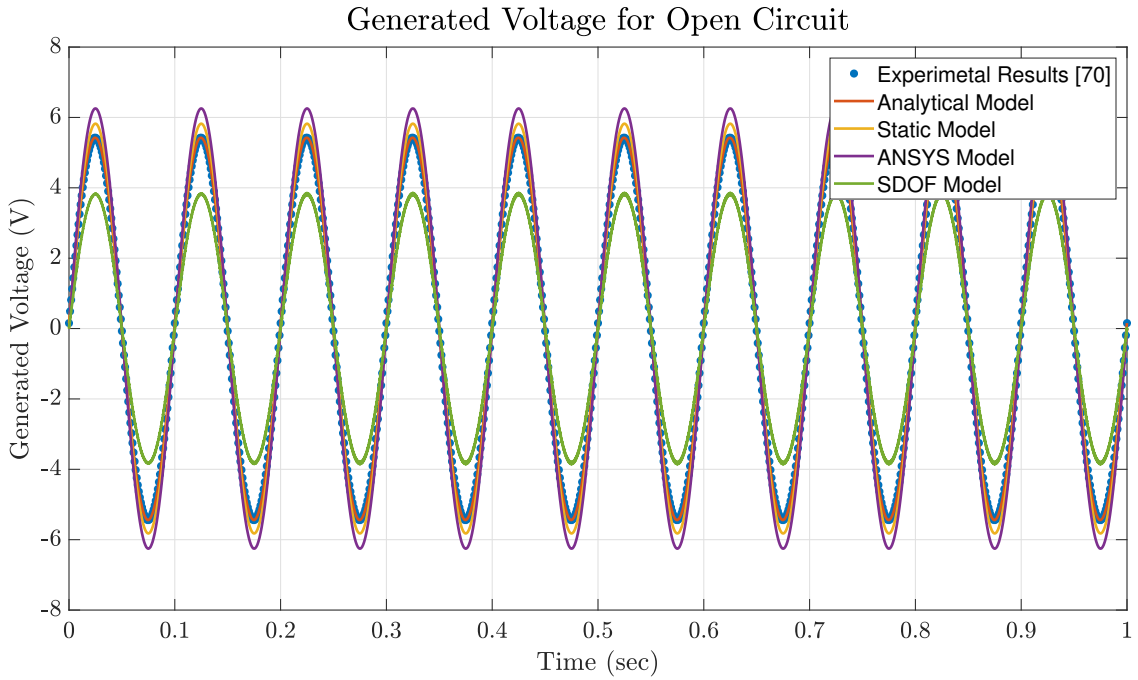

Fig. 30: The generated voltage for the quasi static, SDOF, ANSYS, the distributed parameter models and Experimental Results [70]

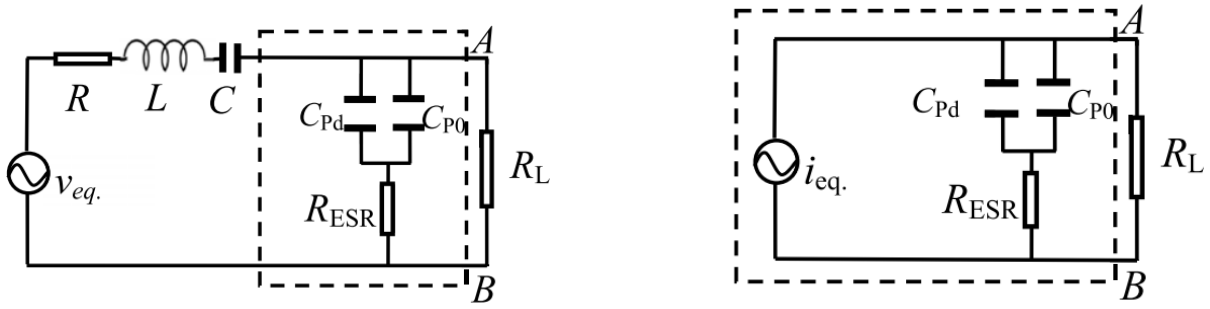

(a) Resonance mode

(b) Off-Resonance mode

Fig. 31: Equivalent circuit for the PZT-Stack connected with a pure resistive load. The dash lined rectangle represents the inside of the PZT-Stack [69]

The R_{ESR} in Fig. (31) stands for Equivalent Serial Resistive and is expressed as

$$R_{ESR} = \frac{tan(\delta)}{\omega C_p}. \tag{170}$$

Further explanation for the circuits shown in Fig. (31) and the symbols can be found in

[69].

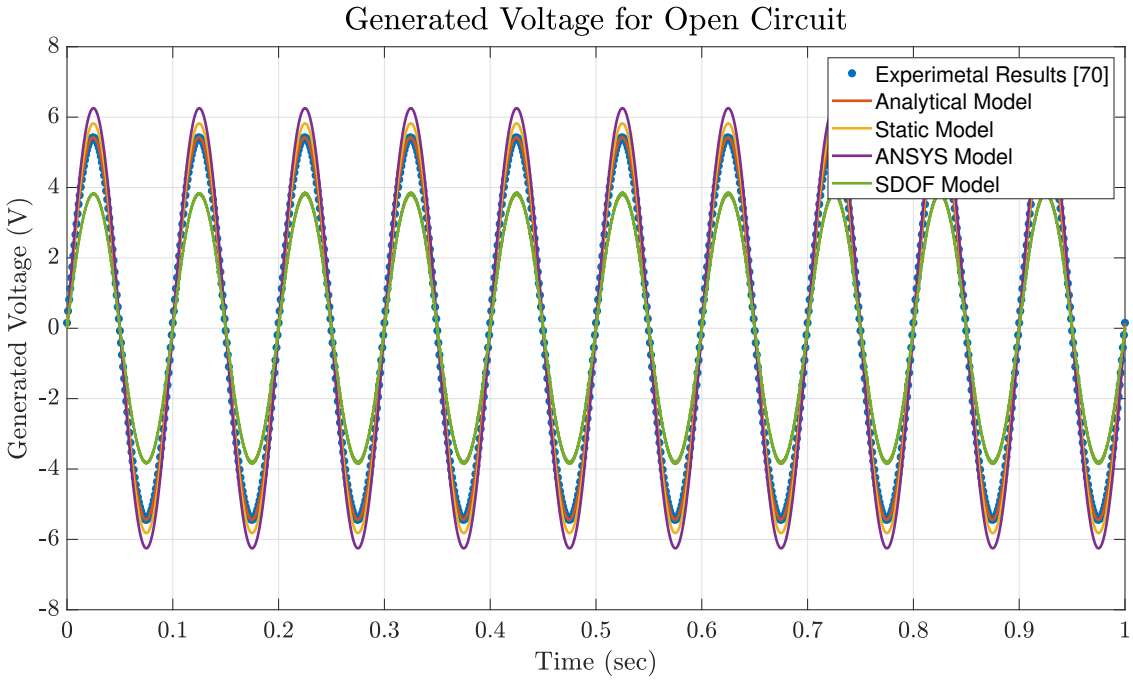

Fig. 32: Generated Voltage for All Models

The ANSYS model, however provided more accurate results compared to the SDOF model with an RMS error $E_{rms} = 15.48.42$. This error can be due to the equivalent capacitance assumption presented by Eq.(99) The finite element model also has discretization errors caused by the mesh and numerical errors of the solution of the FEA.

Although, the static model is the simplest model, and its equation and coding is extremely trivial it gave an error less than the SDOF and the FEA models. It takes almost no computation cost or time. The error was $E_{rms} = 7.7330\%$ which is satisfactory compared to the effort and the complexity of the distributed parameter model.

Table (III) summaries the results for the four models. The second column shows the peak voltage expected by each model. The third column shows the root mean square voltage while the last column shows the errors calculated base on the values of the V_{RMS}.

TABLE III: A Summary of off Resonance Mode Models Result

Model	$V_{max}(Volt)$	$V_{RMS}(Volt)$	$E_{RMS}\%$
Quasi-Static Model	5.824	4.1182	7.7330%
SDOF Model	3.791	2.6806	25.1661%
ANSYS Model	6.243	4.4145	15.4842%
Analytical Model	5.406	3.8226	0.0%

6.2 RESONANCE MODE MODELS RESULTS

This section will start with presenting the results numerically and experimentally of the single stage piezoelectric harvester. Then the second subsection will present certain results from the multistage piezoelectric harvester. Noting that, in this thesis we cannot present all simulated cases and design modifications due to some restrictions imposed on the author by the funding agency.

6.2.1 SINGLE STAGE PIEZOELECTRIC ENERGY HARVESTER

The geometry of the piezoelectric stack and the FPEH are illustrated in Fig. (33), and values of the dimensions are $W_s = h_s = 7mm$, $W = h = 8mm$, $H_{fo} = 17.5mm$, $H_{fi} = 13.5mm$, $L_s = 32.4mm$ and $L_{fo} = 38mm$. The material used to manufacture the stack is 316 Stainless Steel with Modulus of Elasticity $E = 193GPa$ and Poisson's ratio $\nu = 0.27$.

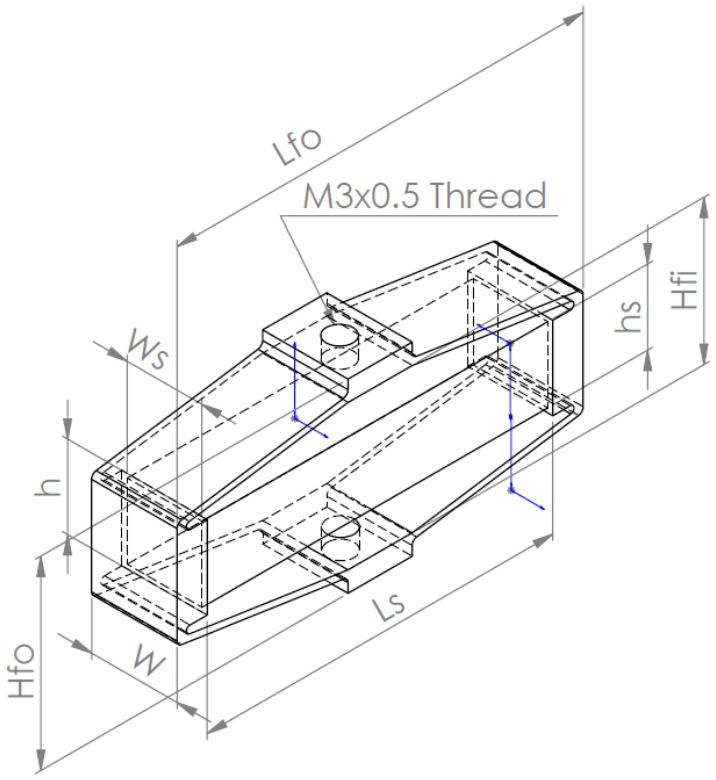

Fig. 33: FPEH Geometry

The full geometry of the stack was modeled. The dimension of the stack is the same as the stack mounted in the FPEH $7 \times 7 \times 32.4mm^3$.

Fig. (34) shows voltage contour plots for the single stage flextensional piezoelectric energy harvester loaded with a 500 *grams* weights and with base excitation of acceleration $1g's$. Fig. (34a) shows the tension cycle while Fig. (34b) shows the compression cycle.

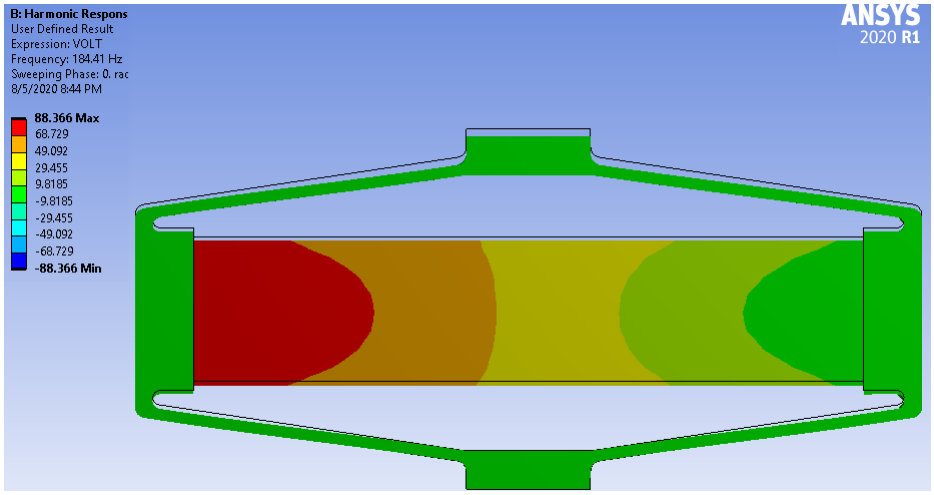

(a)

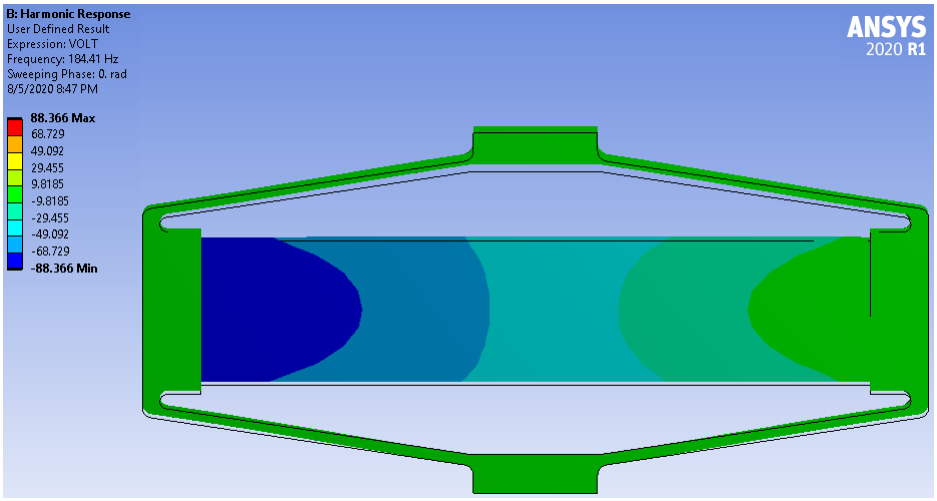

(b)

Fig. 34: Contour plots (a) Tension Cycle (b) Compression Cycle

The monolithic piezoelectric stack actuator (CeramTech SP505) was used in this study as a harvester instead. The stack is built using 300 piezoelectric layers of 0.1 mm thickness sandwiched between 301 silver electrodes. The total volume of the stack is $7mm \times 7mm \times 32.40mm$ and its density is $\rho = 7700kg/m^3$. This is the same piezoelectric multilayer stack used in the off-resonance mode section.

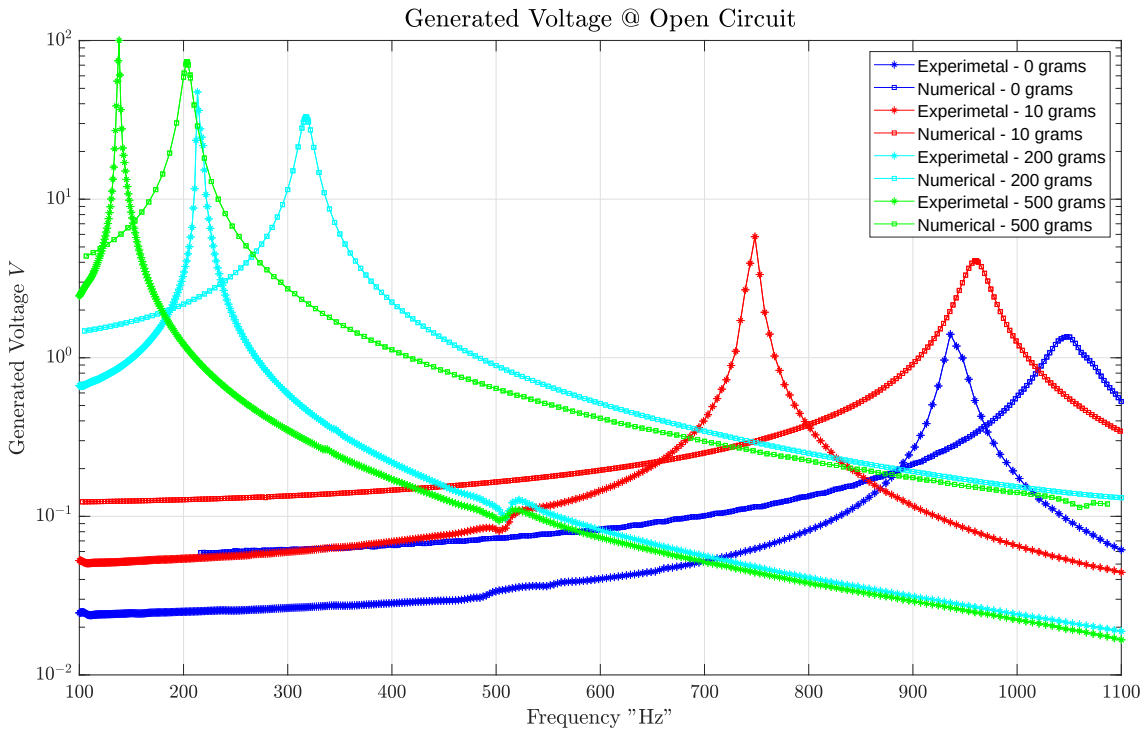

Fig. 35: Voltage Frequency Response Spectra of the FPEH with $1g$ Base Excitation Using Different Proof Masses

6.2.2 MULTI-STAGE FLEXTENSIONAL PIEZOELECTRIC ENERGY HARVESTER

Fig. (36) shows a two stage FPEH, the three multilayer stacks used in that harvester were mainly designed to serve as an actuator. The piezoelectric stacks are model $SM701$, with piezoelectric constant of $d_{33} = 640pC/N$, and dielectric constant of $\varepsilon_{33}^{T} = 3800$ and density of $\rho = 7800kg/m^3$. The force amplification frame was manufactured from $17-4PH$ stainless steel.

In this subsection, we will not delve into the detailed geometry of the harvester because of the restrictions imposed by the company funding this project. Also, not all results will be presented of the same reason.

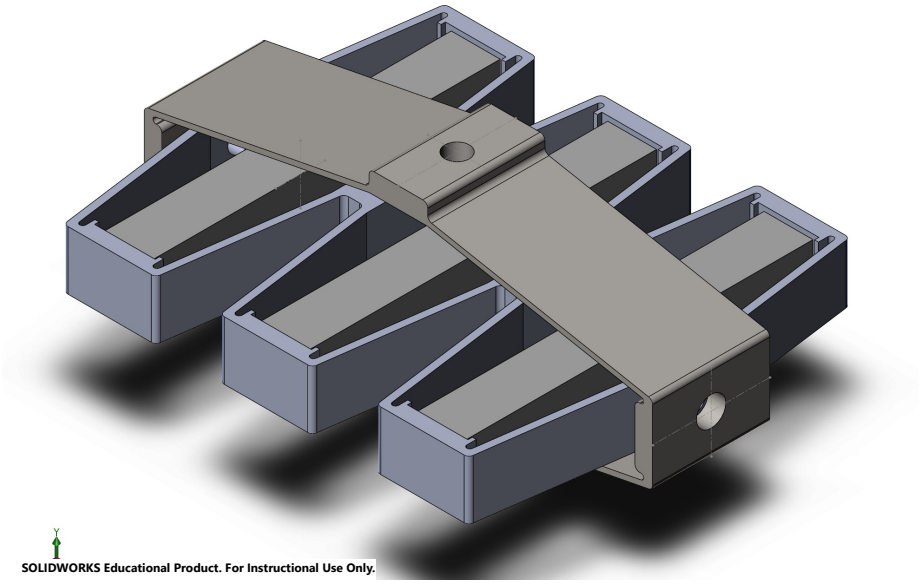

Fig. 36: Multi-Stage Flextensional Energy Harvester

The frequency range applied to the shaker was 170 to 250Hz. The problem with using this setup is that when we attempt to apply a sweep function, at the resonance frequency the energy is sucked suddenly from the shaker and a sudden decrease in the acceleromoter reading is observed as shown in Fig.(37a). Due to the complexity of designing a control algorithm to use the acceleration reading as a feedback and then adjust the output of the shaker such that it maintains fixed acceleration is rather cumbersome. As a result, the experimental results for the voltage output of the will be presented in the results chapter as $Volts/g's$. This is done by dividing the results in Fig. (37a) by the results in Fig. (37b).

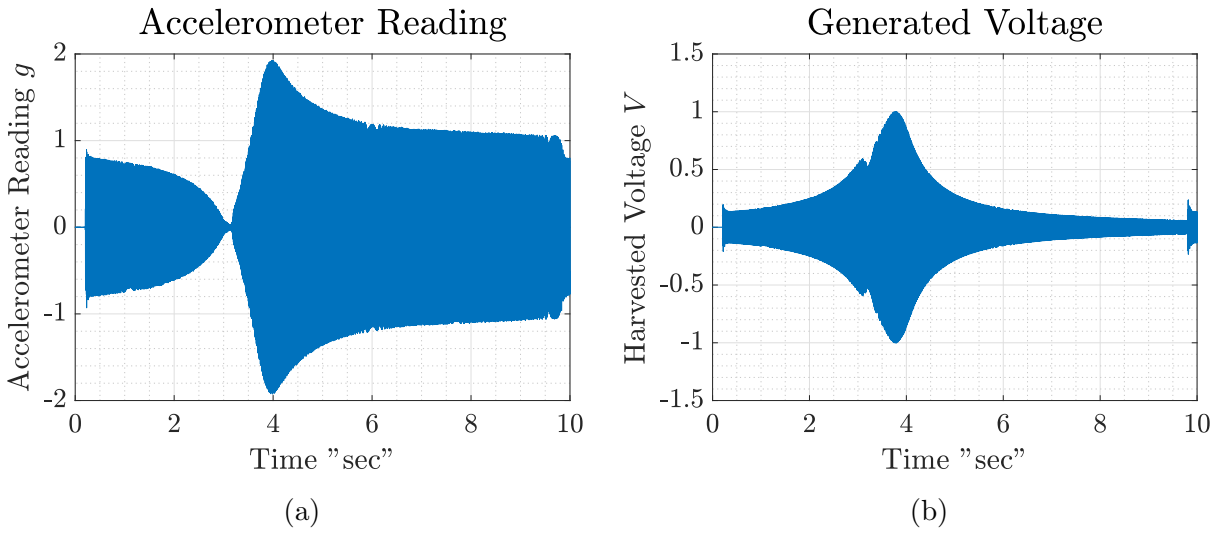

Fig. 37: Experimental Results (a) Accelerometer Feedback (b) Generated Voltage

By applying Fast Fourier Transformation (FFT) to the waveform measured by LAB-VIEW, the spectrum shown in Fig. (38) in the blue line is observed.

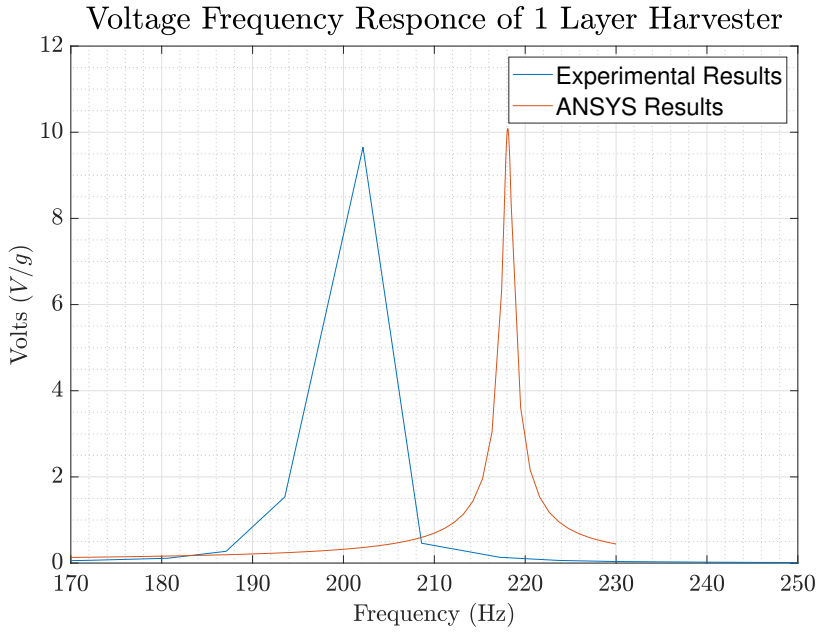

Fig. 38: Multi-Stage Flextensional Energy Harvester

The ANSYS harmonic result is shown in Fig. (38). A damping coefficient of 0.0025 was found to be suitable for that model. This damping coefficient matched the maximum voltage peak of the experimental results. Fig. (39) shows the generated voltage at the resonance

frequency with base excitation of $1g's$ at the maximum and minimum deformations of the harvester; however, the actual harvester was not tested at $1g's$ acceleration because the stress imposed on the second stage frame would be extremely big and would damage the harvester. The actual experiment was performed at an acceleration of $0.1g's$ acceleration.

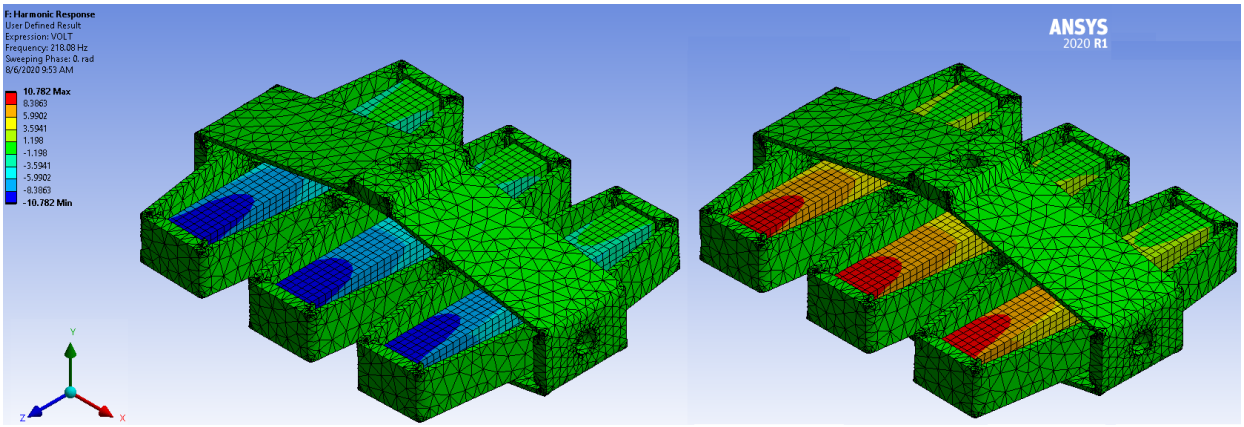

Fig. 39: Multi-Stage FPEH Generated Voltage at base excitation of $1g's$

6.2.3 HARMONIC MODEL DISCUSSION

Figure (35) is the result for this single stage FPEH model. It can be noticed that the experimental results are not in good agreement with the simulated result. Could be differences or flaws in the manufacturing of the actual harvesters due to their extremely small size and finite fillets which affects greatly the harvester's natural frequency and force amplification factor. Also, the assumption of having a piezoelectric bulk object ignores the damping and the stiffness of the 301 silver electrodes as well as the epoxy used to attach the piezoelectric stack to the FAF; which introduces errors to the model. More suspected reasons are mentioned in [119, 91].

For the multistage FPEH, the maximum voltage produced by the harvester in the experiment was $9.65V$ at a resonance frequency of $202.2Hz$, while the maximum voltage produced by the ANSYS model was $10.03V$ at a resonance frequency of $218Hz$ as shown in Fig. (38).

The error in the resonance frequency detection by the ANSYS model can be caused by

the fact that the fillets and dimensions of the harvester's frames are extremely small. This makes the manufacturing process prone to minor errors which lead to a shift in the deviation of the manufactured harvester compared to the designed one. Also, there can be a mismatch between the material properties used to manufacture the frame compared to the material properties specified in the data sheets used in the ANSYS model.

The flextensional piezoelectric energy harvesters have small curvatures and fillets, these regions are considered stress concentration points. Accordingly, the stresses should be checked and quantified in these regions before putting these harvesters in service. The maximum stress produced in in the single stage flextensional piezoelectric energy harvester is $5.43MPa$ (as shown in Fig. (40))which is much lower than the yield stress of the material used in manufacturing the FAF ($\sigma_{yield} = 290MPa$)

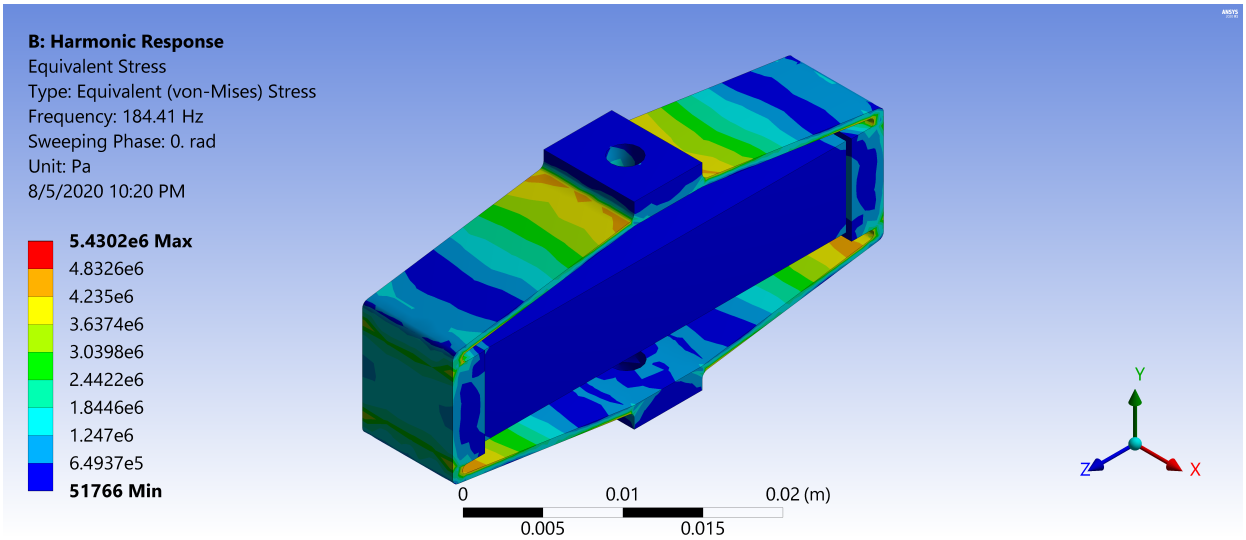

Fig. 40: Von-mises Stress contour plot for the stresses applied on the Single stage FPEH when loaded with 500 $grams$ at resonance frequency with magnitude $1g's$

Fig. (41) shows the stress distribution on the multistage energy harvester at base excitation of $0.1g's$. It can be seen that the maximum stress occurs in the area of contact between the first stage and second stage frames.

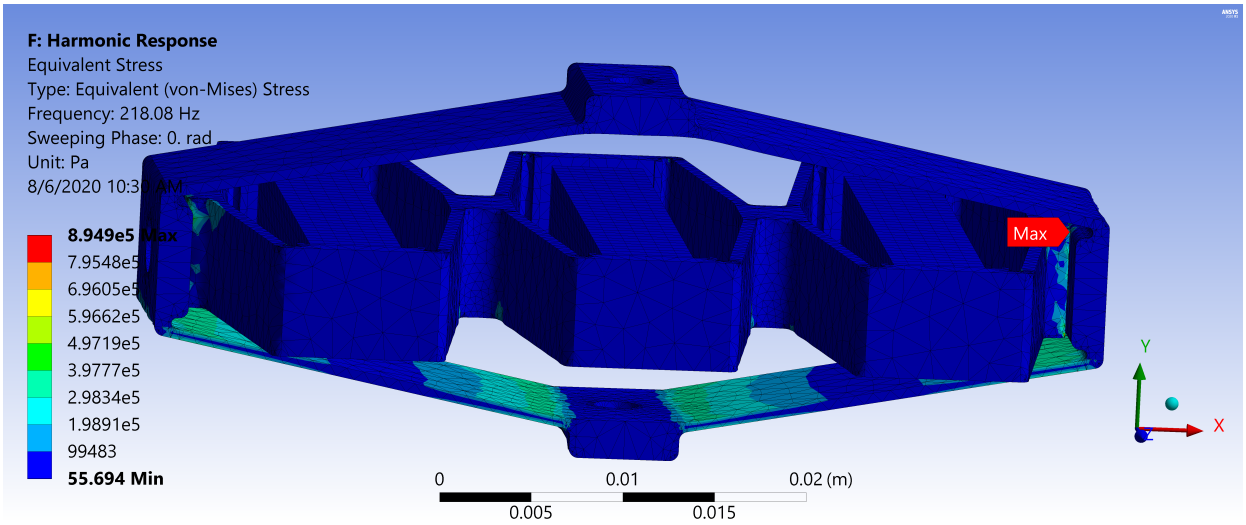

Fig. 41: Multi-Stage FPEH stress distribution at base excitation of $0.1g's$

CHAPTER 7

SUMMARY AND FUTURE WORK

For the resonance mode, the recommended model for simulation is the static model, as it has the least programming complexity and minimal computational time compared to the other investigated models. The distributed parameter model gives the most accurate result with almost zero error. This is because the model accounts for the difference in strain distribution along the piezoelectric stack compared to the other models. The SDOF model gave the maximum deviation compared to the experimental data. This is because the SDOF model treats the multilayer stack as a point mass. Also, the SDOF model ignores the damping inside the piezoelectric stack caused by the presence of the electrodes, and it ignored the strains distribution or the difference in strains between the piezoelectric layers. The finite element model produced a satisfactory result, but the static model produced less error.

The operation of piezoelectric energy harvesters in resonance mode produces significantly high voltage compared to the off-resonance mode. However, the design of the resonance mode harvesters is challenging because of the higher stresses imposed on the frame at such frequencies. The deviation in the resonance frequency between the ANSYS model and the experimental reading can be caused by the fact that the fillets and dimensions of the harvester's frames are extremely small. This makes the manufacturing process prone to minor errors which leads to a shift in the deviation of the manufactured harvester compared to the designed one. Also, there can be a mismatch between the material properties used to manufacture the frame compared to the material properties specified in the data sheets used in the ANSYS model.

In the future, this study can be extended to investigate numerical methods (such as the Transfer Function method) in resonance mode. The performance of the Single Degree of

Freedom model, the Finite Element model and the Distributed Parameter model have to be tested for various resistive loads and in resonance mode as well as. Also, an exact replication of this thesis can be done but for flextensional piezoelectric actuators instead of harvesters.

REFERENCES

[1] X. Tang, X. Wang, R. Cattley, F. Gu, and A. D. Ball, "Energy harvesting technologies for achieving self-powered wireless sensor networks in machine condition monitoring: A review," *Sensors*, vol. 18, no. 12, p. 4113, 2018.

[2] A. Abdelkefi, M. R. Hajj, and A. H. Nayfeh, "Phenomena and modeling of piezoelectric energy harvesting from freely oscillating cylinders," *Nonlinear Dynamics*, vol. 70, pp. 1377–1388, Oct 2012.

[3] T. Huesgen, P. Woias, and N. Kockmann, "Design and fabrication of mems thermoelectric generators with high temperature efficiency," *Sensors and Actuators A: Physical*, vol. 145, pp. 423–429, 2008.

[4] B. C. Norman, "Power options for wireless sensor networks," *IEEE Aerospace and Electronic Systems Magazine*, vol. 22, no. 4, pp. 14–17, 2007.

[5] A. Abdelkefi, *Global nonlinear analysis of piezoelectric energy harvesting from ambient and aeroelastic vibrations*. PhD thesis, Virginia Tech, 2012.

[6] H. Abdelmoula and A. Abdelkefi, "Ultra-wide bandwidth improvement of piezoelectric energy harvesters through electrical inductance coupling," *The European Physical Journal Special Topics*, vol. 224, no. 14-15, pp. 2733–2753, 2015.

[7] S. P. Beeby, M. J. Tudor, and N. White, "Energy harvesting vibration sources for microsystems applications," *Measurement science and technology*, vol. 17, no. 12, p. R175, 2006.

[8] A. Abdelkefi and N. Barsallo, "Comparative modeling of low-frequency piezomagnetoelastic energy harvesters," *Journal of Intelligent Material Systems and Structures*, vol. 25, no. 14, pp. 1771–1785, 2014.

[9] M. Shabara, A. Rahman Badawi, and T.-B. Xu, "Comprehensive piezoelectric material application issues on energy harvesting for artificial intelligence systems," in *AIAA Scitech 2020 Forum*, p. 1862, 2020.

[10] A. Abdelkefi, "Aeroelastic energy harvesting: A review," *International Journal of Engineering Science*, vol. 100, pp. 112–135, 2016.

[11] S. R. Anton and H. A. Sodano, "A review of power harvesting using piezoelectric materials (2003–2006)," *Smart materials and Structures*, vol. 16, no. 3, p. R1, 2007.

[12] K. A. Cook-Chennault, N. Thambi, and A. M. Sastry, "Powering mems portable devices—a review of non-regenerative and regenerative power supply systems with special emphasis on piezoelectric energy harvesting systems," *Smart materials and structures*, vol. 17, no. 4, p. 043001, 2008.

[13] A. Erturk and D. J. Inman, *Piezoelectric energy harvesting*. John Wiley & Sons, 2011.

[14] R. L. Harne and K. Wang, "A review of the recent research on vibration energy harvesting via bistable systems," *Smart materials and structures*, vol. 22, no. 2, p. 023001, 2013.

[15] D. P. Arnold, "Review of microscale magnetic power generation," *IEEE Transactions on Magnetics*, vol. 43, no. 11, pp. 3940–3951, 2007.

[16] P. Glynne-Jones, M. J. Tudor, S. P. Beeby, and N. M. White, "An electromagnetic, vibration-powered generator for intelligent sensor systems," *Sensors and Actuators A: Physical*, vol. 110, no. 1-3, pp. 344–349, 2004.

[17] M. A. Karami, *Micro-scale and nonlinear vibrational energy harvesting*. PhD thesis, Virginia Tech, 2012.

[18] P. D. Mitcheson, P. Miao, B. H. Stark, E. Yeatman, A. Holmes, and T. Green, "Mems electrostatic micropower generator for low frequency operation," *Sensors and Actuators A: Physical*, vol. 115, no. 2-3, pp. 523–529, 2004.

[19] A. Toprak and O. Tigli, "Piezoelectric energy harvesting: State-of-the-art and challenges," *Applied Physics Reviews*, vol. 1, no. 3, p. 031104, 2014.

[20] E. J. R. Company, "Demonstration experiment of the "power-generating floor" at tokyo station," 2008.

[21] J. Wang, Z. Shi, H. Xiang, and G. Song, "Modeling on energy harvesting from a railway system using piezoelectric transducers," *Smart Materials and Structures*, vol. 24, no. 10, p. 105017, 2015.

[22] S. Saadon and O. Sidek, "A review of vibration-based mems piezoelectric energy harvesters," *Energy Conversion and Management*, vol. 52, no. 1, pp. 500–504, 2011.

[23] N. E. Dutoit, B. L. Wardle, and S.-G. Kim, "Design considerations for mems-scale piezoelectric mechanical vibration energy harvesters," *Integrated ferroelectrics*, vol. 71, no. 1, pp. 121–160, 2005.

[24] H. Yu, J. Zhou, L. Deng, and Z. Wen, "A vibration-based mems piezoelectric energy harvester and power conditioning circuit," *Sensors*, vol. 14, no. 2, pp. 3323–3341, 2014.

[25] W. Choi, Y. Jeon, J.-H. Jeong, R. Sood, and S.-G. Kim, "Energy harvesting mems device based on thin film piezoelectric cantilevers," *Journal of Electroceramics*, vol. 17, no. 2-4, pp. 543–548, 2006.

[26] J. Briscoe and S. Dunn, "Piezoelectric nanogenerators–a review of nanostructured piezoelectric energy harvesters," *Nano Energy*, vol. 14, pp. 15–29, 2015.

[27] I. Dakua and N. Afzulpurkar, "Piezoelectric energy generation and harvesting at the nano-scale: materials and devices," *Nanomaterials and Nanotechnology*, vol. 3, p. 21, 2013.

[28] Y. Suzuki, "Recent progress in mems electret generator for energy harvesting," *IEEJ Transactions on Electrical and Electronic Engineering*, vol. 6, no. 2, pp. 101–111, 2011.

[29] S. J. Russell and P. Norvig, *Artificial intelligence: a modern approach*. Malaysia; Pearson Education Limited,, 2016.

[30] A. Mellit and S. A. Kalogirou, "Artificial intelligence techniques for photovoltaic applications: A review," *Progress in energy and combustion science*, vol. 34, no. 5, pp. 574–632, 2008.

[31] M. Hilbert and P. López, "The world's technological capacity to store, communicate, and compute information," *Science*, vol. 332, no. 6025, pp. 60–65, 2011.

[32] P. Zikopoulos, C. Eaton, *et al.*, *Understanding big data: Analytics for enterprise class hadoop and streaming data*. McGraw-Hill Osborne Media, 2011.

[33] A. McAfee, E. Brynjolfsson, T. H. Davenport, D. Patil, and D. Barton, "Big data: the management revolution," *Harvard business review*, vol. 90, no. 10, pp. 60–68, 2012.

[34] C. Zhang, W. Zou, L. Ma, and Z. Wang, "Biologically inspired jumping robots: A comprehensive review," *Robotics and Autonomous Systems*, 2019.

[35] D. N. Nenchev, A. Konno, and T. Tsujita, *Humanoid Robots: Modeling and Control*. Butterworth-Heinemann, 2018.

[36] C. Breazeal, "Emotion and sociable humanoid robots," *International journal of human-computer studies*, vol. 59, no. 1-2, pp. 119–155, 2003.

[37] K. Ashton *et al.*, "That 'internet of things' thing," *RFID journal*, vol. 22, no. 7, pp. 97–114, 2009.

[38] F. Xia, L. T. Yang, L. Wang, and A. Vinel, "Internet of things," *International Journal of Communication Systems*, vol. 25, no. 9, p. 1101, 2012.

[39] S. W. Arms, C. Townsend, D. Churchill, J. Galbreath, and S. Mundell, "Power management for energy harvesting wireless sensors," in *Smart Structures and Materials 2005: Smart Electronics, MEMS, BioMEMS, and Nanotechnology*, vol. 5763, pp. 267–275, International Society for Optics and Photonics, 2005.

[40] S. Roundy, "On the effectiveness of vibration-based energy harvesting," *Journal of Intelligent Material Systems and Structures*, vol. 16, no. 10, pp. 809–823, 2005.

[41] C.-Y. Sue and N.-C. Tsai, "Human powered mems-based energy harvest devices," *Applied Energy*, vol. 93, pp. 390–403, 2012.

[42] K. Uchino, "Piezoelectric actuators 2006," *Journal of Electroceramics*, vol. 20, no. 3-4, pp. 301–311, 2008.

[43] B. Jaffe, *Piezoelectric ceramics*, vol. 3. Elsevier, 2012.

[44] T. Zheng, J. Wu, D. Xiao, and J. Zhu, "Recent development in lead-free perovskite piezoelectric bulk materials," *Progress in materials science*, vol. 98, pp. 552–624, 2018.

[45] T. Karaki, K. Yan, T. Miyamoto, and M. Adachi, "Lead-free piezoelectric ceramics with large dielectric and piezoelectric constants manufactured from batio3 nanopowder," *Japanese Journal of Applied Physics*, vol. 46, no. 2L, p. L97, 2007.

[46] B. Jaffe, R. Roth, and S. Marzullo, "Piezoelectric properties of lead zirconate-lead titanate solid-solution ceramics," *Journal of Applied Physics*, vol. 25, no. 6, pp. 809–810, 1954.

[47] L. Cross and R. Newnham, "History of ferroelectrics," *Ceramics and Civilization*, vol. 3, pp. 289–305, 1987.

[48] L. A. Pautov, A. A. Agakhanov, E. Sokolova, and F. C. Hawthorne, "Maleevite, bab2si2o8, and pekovite, srb2si2o8, new mineral species from the dara-i-pioz alkaline massif, northern tajikistan: description and crystal structure," *The Canadian Mineralogist*, vol. 42, no. 1, pp. 107–119, 2004.

[49] B. Bhushan, *Scanning probe microscopy in nanoscience and nanotechnology 2*. Springer Science & Business Media, 2010.

[50] S. E. E. Park, V. Vedula, M.-J. Pan, W. S. Hackenberger, P. Pertsch, and T. R. Shrout, "Relaxor-based ferroelectric single crystals for electromechanical actuators," in *Smart Structures and Materials 1998: Smart Materials Technologies*, vol. 3324, pp. 136–144, International Society for Optics and Photonics, 1998.

[51] S.-E. Park and T. R. Shrout, "Relaxor based ferroelectric single crystals for electromechanical actuators," *Materials Research Innovations*, vol. 1, no. 1, pp. 20–25, 1997.

[52] S. Zhang, J. Luo, W. Hackenberger, and T. R. Shrout, "Characterization of pb (in 1/2 nb 1/2) o 3–pb (mg 1/3 nb 2/3) o 3–pbtio 3 ferroelectric crystal with enhanced phase transition temperatures," *Journal of applied physics*, vol. 104, no. 6, p. 064106, 2008.

[53] Z.-Y. Cheng, V. Bharti, T.-B. Xu, H. Xu, T. Mai, and Q. Zhang, "Electrostrictive poly (vinylidene fluoride-trifluoroethylene) copolymers," *Sensors and Actuators A: Physical*, vol. 90, no. 1-2, pp. 138–147, 2001.

[54] Q. Zhang, S. Zhang, A. Cheng, S. Liu, B. Zellers, and D. Anderson, "Relaxor ferroelectric eaps and their applications," *Nature*, pp. 2002–2010, 2011.

[55] Harrison and Ounaies, "Piezoelectric polymers," *NASA/CR-2001-211422/ ICASE Report No. 2001-43*, 2001.

[56] H. W. Kim, S. Priya, K. Uchino, and R. E. Newnham, "Piezoelectric energy harvesting under high pre-stressed cyclic vibrations," *Journal of Electroceramics*, vol. 15, no. 1, pp. 27–34, 2005.

[57] H. Kim, S. Priya, and K. Uchino, "Modeling of piezoelectric energy harvesting using cymbal transducers," *Japanese journal of applied physics*, vol. 45, no. 7R, p. 5836, 2006.

[58] K. Uchino and T. Ishii, "Energy flow analysis in piezoelectric energy harvesting systems," *Ferroelectrics*, vol. 400, no. 1, pp. 305–320, 2010.

[59] J. Yuan, X. Shan, T. Xie, and W. Chen, "Modeling and improvement of a cymbal transducer in energy harvesting," *Journal of Intelligent Material Systems and Structures*, vol. 21, no. 8, pp. 765–771, 2010.

[60] J. Palosaari, M. Leinonen, J. Hannu, J. Juuti, and H. Jantunen, "Energy harvesting with a cymbal type piezoelectric transducer from low frequency compression," *Journal of electroceramics*, vol. 28, no. 4, pp. 214–219, 2012.

[61] A. Dogan, J. Tressler, and R. E. Newnham, "Solid-state ceramic actuator designs," *AIAA journal*, vol. 39, no. 7, pp. 1354–1362, 2001.

[62] T.-B. Xu, "Energy harvesting using piezoelectric materials in aerospace structures," in *Structural Health Monitoring (SHM) in Aerospace Structures*, pp. 175–212, Elsevier, 2016.

[63] K. Deng and K. Andic, "Piezoelectric vibration energy harvesting device," June 23 2005. US Patent App. 11/031,993.

[64] O. Sosnicki, N. Lhermet, and F. Claeyssen, "Vibration energy harvesting in aircraft using piezoelectric actuators," in *Proc Actuator*, pp. 968–971, 2006.

[65] T.-b. Xu and l. Zuo, "Key issues on flextensional piezoelectric energy harvester deveoplments," in *ASME 2019 International Design Engineering Technical Conferences and Computer and Information in Engineering Conference*, American Society of Mechanical Engineers Digital Collection, 2019.

[66] W. Liu, A. Badel, F. Formosa, Y. Wu, and A. Agbossou, "Novel piezoelectric bistable oscillator architecture for wideband vibration energy harvesting," *Smart materials and structures*, vol. 22, no. 3, p. 035013, 2013.

[67] W. Q. Liu, A. Badel, F. Formosa, Y. P. Wu, and A. Agbossou, "Wideband energy harvesting using a combination of an optimized synchronous electric charge extraction circuit and a bistable harvester," *Smart Materials and Structures*, vol. 22, no. 12, p. 125038, 2013.

[68] N. Bencheikh, A. Pagès, T. Forissier, T. Porchez, A. Kras, A. Badel, and F. Formosa, "A bistable piezoelectric harvester for wideband mechanical frequency excitation," in *ACTUATOR*, pp. PP–51, 2014.

[69] T.-B. Xu, E. J. Siochi, J. H. Kang, L. Zuo, W. Zhou, X. Tang, and X. Jiang, "Energy harvesting using a pzt ceramic multilayer stack," *Smart Materials and Structures*, vol. 22, no. 6, p. 065015, 2013.

[70] F. Qian, T.-B. Xu, *et al.*, "A distributed parameter model for the piezoelectric stack harvester subjected to general periodic and random excitations," *Engineering Structures*, vol. 173, pp. 191–202, 2018.

[71] T. Starner, "Human-powered wearable computing," *IBM systems Journal*, vol. 35, no. 3.4, pp. 618–629, 1996.

[72] N. S. Shenck and J. A. Paradiso, "Energy scavenging with shoe-mounted piezoelectrics," *IEEE micro*, no. 3, pp. 30–42, 2001.

[73] J. Kymissis, C. Kendall, J. Paradiso, and N. Gershenfeld, "Parasitic power harvesting in shoes," in *Digest of Papers. Second International Symposium on Wearable Computers (Cat. No. 98EX215)*, pp. 132–139, IEEE, 1998.

[74] F. Qian, T.-B. Xu, and L. Zuo, "Material equivalence, modeling and experimental validation of a piezoelectric boot energy harvester," *Smart Materials and Structures*, vol. 28, no. 7, p. 075018, 2019.

[75] F. Qian, T.-B. Xu, and L. Zuo, "Design, optimization, modeling and testing of a piezoelectric footwear energy harvester," *Energy conversion and management*, vol. 171, pp. 1352–1364, 2018.

[76] R. Baghbani and M. Ashoorirad, "A power generating system for mobile electronic devices using human walking motion," in *2009 Second International Conference on Computer and Electrical Engineering*, vol. 2, pp. 385–388, Dec 2009.

[77] N. S. Shenck, *A demonstration of useful electric energy generation from piezoceramics in a shoe*. PhD thesis, Massachusetts Institute of Technology, 1999.

[78] L. C. Rome, L. Flynn, E. M. Goldman, and T. D. Yoo, "Generating electricity while walking with loads," *Science*, vol. 309, no. 5741, pp. 1725–1728, 2005.

[79] J. Granstrom, J. Feenstra, H. A. Sodano, and K. Farinholt, "Energy harvesting from a backpack instrumented with piezoelectric shoulder straps," *Smart Materials and Structures*, vol. 16, no. 5, p. 1810, 2007.

[80] J. Palosaari, M. Leinonen, J. Juuti, J. Hannu, and H. Jantunen, "Piezoelectric circular diaphragm with mechanically induced pre-stress for energy harvesting," *Smart Materials and Structures*, vol. 23, no. 8, p. 085025, 2014.

[81] C. Mo, L. J. Radziemski, and W. W. Clark, "Experimental validation of energy harvesting performance for pressure-loaded piezoelectric circular diaphragms," *Smart Materials and structures*, vol. 19, no. 7, p. 075010, 2010.

[82] M. Leinonen, J. Palosaari, J. Juuti, and H. Jantunen, "Combined electrical and electromechanical simulations of a piezoelectric cymbal harvester for energy harvesting from walking," *Journal of Intelligent Material Systems and Structures*, vol. 25, no. 4, pp. 391–400, 2014.

[83] W. Wang, T. Yang, X. Chen, and X. Yao, "Vibration energy harvesting using a piezoelectric circular diaphragm array," *IEEE transactions on ultrasonics, ferroelectrics, and frequency control*, vol. 59, no. 9, pp. 2022–2026, 2012.

[84] X.-r. Chen, T.-q. Yang, W. Wang, and X. Yao, "Vibration energy harvesting with a clamped piezoelectric circular diaphragm," *Ceramics International*, vol. 38, pp. S271–S274, 2012.

[85] S. Ballantine, "A piezo-electric loud speaker for the higher audio frequencies," *Proceedings of the Institute of Radio Engineers*, vol. 21, no. 10, pp. 1399–1408, 1933.

[86] C. B. Sawyer, "The use of rochelle salt crystals for electrical reproducers and microphones," *Proceedings of the Institute of Radio Engineers*, vol. 19, no. 11, pp. 2020–2029, 1931.

[87] C. J. Morris and F. K. Forster, "Optimization of a circular piezoelectric bimorph for a micropump driver," *Journal of Micromechanics and Microengineering*, vol. 10, no. 3, p. 459, 2000.

[88] E.-H. Yang and D. V. Wiberg, "A wafer-scale membrane transfer process for the fabrication of optical quality, large continuous membranes," *Journal of microelectromechanical systems*, vol. 12, no. 6, pp. 804–815, 2003.

[89] Z. Xiao, T. q. Yang, Y. Dong, and X. c. Wang, "Energy harvester array using piezoelectric circular diaphragm for broadband vibration," *Applied Physics Letters*, vol. 104, no. 22, p. 223904, 2014.

[90] M. Deterre, E. Lefeuvre, and E. Dufour-Gergam, "An active piezoelectric energy extraction method for pressure energy harvesting," *Smart Materials and Structures*, vol. 21, no. 8, p. 085004, 2012.

[91] T.-B. Xu, X. Jiang, and J. Su, "A piezoelectric multilayer-stacked hybrid actuation/transduction system," *Applied Physics Letters*, vol. 98, no. 24, p. 243503, 2011.

[92] T.-B. Xu, X. Jiang, and J. Su, "Piezoelectric multilayer-stacked hybrid actuation/transduction system," Mar. 25 2014. US Patent 8,680,749.

[93] T.-B. Xu, X. Jiang, J. Su, P. W. Rehrig, and W. S. Hackenberger, "Hybrid piezoelectric energy harvesting transducer system," Nov. 4 2008. US Patent 7,446,459.

[94] T.-B. Xu, E. J. Siochi, L. Zuo, X. Jiang, and J. H. Kang, "Multistage force amplification of piezoelectric stacks," June 2 2015. US Patent 9,048,759.

[95] A. Meitzler, H. Tiersten, A. Warner, D. Berlincourt, G. Couqin, and F. Welsh III, "Ieee standard on piezoelectricity "ansi/ieee std 176–1987"," *The Institute of Electrical and Electronics Engineers Inc*, 1987.

[96] M. Goldfarb and N. Celanovic, "Modeling piezoelectric stack actuators for control of micromanipulation," *IEEE Control Systems Magazine*, vol. 17, no. 3, pp. 69–79, 1997.

[97] J. J. Stoker, *Nonlinear elasticity*. Gordon and Breach, 1968.

[98] C. J. Brennan, "A physical model for the electrical hysteresis of thin-film ferroelectric capacitors," *Ferroelectrics*, vol. 132, no. 1, pp. 245–257, 1992.

[99] J. S. P., "Constitutive models for piezoelectric materials, constitutive laws for engineering materials: Recent advances and industrial applications," pp. 605–8, New York: ASME, 1991.

[100] S. P. Joshi, "Non-linear constitutive relations for piezoceramic materials," *Smart Materials and Structures*, vol. 1, no. 1, p. 80, 1992.

[101] K. Uchino, *Ferroelectric devices*. Second Edition, CRC press, 2018.

[102] P. A. Tipler and G. Mosca, *Physics for scientists and engineers*. Macmillan, 2007.

[103] D. Boussaa, "On thermodynamic potentials in thermoelasticity under small strain and finite thermal perturbation assumptions," *International Journal of Solids and Structures*, vol. 51, no. 1, pp. 26–34, 2014.

[104] A. Porporato, S. Calabrese, and T. Hueckel, "Thermodynamic relations among isotropic material properties in conditions of plane shear stress," *Entropy*, vol. 21, no. 3, p. 295, 2019.

[105] L. APC International, *Piezoelectric ceramics: principles and applications*. APC International, 2002.

[106] D. Damjanovic, "Ferroelectric, dielectric and piezoelectric properties of ferroelectric thin films and ceramics," *Reports on Progress in Physics*, vol. 61, no. 9, p. 1267, 1998.

[107] L. APC International, *Piezoelectric Ceramics: Principles and Applications*. APC International, 2011.

[108] "Properties of piezoceramic material at high field." `http://www.noliac.com/tutorials/piezo-basics/properties-of-piezoceramic-material-at-high-field`.

[109] R. Ash, *MAE 607 - Continuum Mechanics Lectrue Notes*. Old Dominion University, 2018.

[110] J. Feenstra, J. Granstrom, and H. Sodano, "Energy harvesting through a backpack employing a mechanically amplified piezoelectric stack," *Mechanical Systems and Signal Processing*, vol. 22, no. 3, pp. 721–734, 2008.

[111] M. Goldfarb and N. Celanovic, "Modeling piezoelectric stack actuators for control of micromanipulation," *IEEE Control Systems Magazine*, vol. 17, pp. 69–79, June 1997.

[112] D. Croft, D. McAllister, and S. Devasia, "High-speed scanning of piezo-probes for nano-fabrication," *Journal of manufacturing science and engineering*, vol. 120, no. 3, pp. 617–622, 1998.

[113] J. Park and W. Moon, "Hysteresis compensation of piezoelectric actuators: The modified rayleigh model," *Ultrasonics*, vol. 50, no. 3, pp. 335–339, 2010.

[114] S. Neiss, F. Goldschmidtboeing, M. Kroener, and P. Woias, "Analytical model for nonlinear piezoelectric energy harvesting devices," *Smart Materials and Structures*, vol. 23, no. 10, p. 105031, 2014.

[115] D. A. Ochoa, J. A. Casals, M. Venet, J.-C. M'Peko, and J. E. García, "Dielectric and piezoelectric nonlinear properties of slightly textured lead barium niobate ceramics," *Journal of Applied Physics*, vol. 125, no. 2, p. 024101, 2019.

[116] C. M. Landis, "Non-linear constitutive modeling of ferroelectrics," *Current Opinion in Solid State and Materials Science*, vol. 8, no. 1, pp. 59–69, 2004.

[117] T. D. Leigh and D. C. Zimmerman, "An implicit method for the nonlinear modelling and simulation of piezoceramic actuators displaying hysteresis," in *Smart structures and materials*, pp. 57–63, 1991.

[118] P. Ge and M. Jouaneh, "Modeling hysteresis in piezoceramic actuators," *Precision engineering*, vol. 17, no. 3, pp. 211–221, 1995.

[119] L. Tolliver, T.-B. Xu, and X. Jiang, "Finite element analysis of the piezoelectric stacked-hybats transducer," *Smart materials and structures*, vol. 22, no. 3, p. 035015, 2013.

VITA

Mohamed A. Shabara
Department of Mechanical and Aerospace Engineering
Old Dominion University
Norfolk, VA 23529

Mohamed Shabara was born in Alexandria, Egypt. He completed his Bachelors of Science in Mechanical Engineering in 2013 from the Department of Mechanical Engineering, Alexandria University, Egypt. After his graduation worked in the oil and gas field as an Offshore Gas turbines Engineer, then as an off Senior Gas Turbines Engineer in Abu Qir Petroleum Company (WEPCO). During his work he gained professional experience with gas turbines, turbo-expanders, control systems (PLC), turbo-compressors, gas conditioning and processing. He also received the certified vibration analyst certification CAT II from the vibration Institute in USA.

Mohamed Shabara received his first Master of Science Degree in 2018 from the Department of Mechanical Engineering, Alexandria University, Egypt. His Master Dissertation in Alexandria University was in Fluid Structure Interaction and Flow Induced Vibrations. During that time he worked with computation fluid dynamics approaches, finite element analysis and vibrations.

In Spring 2019, Mr. Mohamed Shabara got an opportunity to pursue a graduate degree in Old Dominion University in the Smart Materials and Intelligent Devices Lab under the supervision of Prof. Tiang-Bing Xu. Accordingly, he took a leave from Abu Qir Petroleum Company and moved to the US to study in Old Dominion University. Starting from Fall 2020, Mohamed started pursuing his PhD in Iowa State University in the Aerospace Engineering Department.

Typeset using LaTeX.